

Research Paper

An efficient nonlinear octree SBFEM and its application to complicated geotechnical structures

Kai Chen, Degao Zou*, Xianjing Kong, Xiang Yu

The State Key Laboratory of Coastal and Offshore Engineering, Dalian University of Technology, Dalian, Liaoning 116024, China
 School of Hydraulic Engineering, Dalian University of Technology, Dalian, Liaoning 116024, China

ARTICLE INFO

Keywords:

Elasto-plastic analysis
 Scaled boundary finite element method
 Complex geotechnical structures

ABSTRACT

An efficient nonlinear octree scaled boundary finite element method (SBFEM) is proposed to improve the ability of the SBFEM to analyse complicated structures. The polygon boundaries are directly solved using a pre-calculated mean-value interpolation. The nonlinearity can be considered via an internal quadratic tetrahedral integral scheme. Three simulations are performed to evaluate the accuracy, versatility, flexibility and high efficiency of the method. The difficulties of automatic modelling for both layered construction and material partitioning are eliminated using the octree meshing algorithm. The proposed method can serve as a powerful technique for the rapid design and analysis of geotechnical structures.

1. Introduction

The displacement-based finite element method (FEM) is the pre-eminent numerical method for applications in engineering due to its many desirable features; for instance, arbitrarily complex geometries can be accommodated with a single algorithmic design, and a high solution precision can be obtained with acceptable computational effort.

However, the conventional types of finite elements used in three-dimensional problems are hexahedrons, tetrahedrons, wedges and pyramids. The mesh used in the method must conform to the boundary of the problem domain, which leads to difficulty in solving many complex problems in modern applications. These types of problems can be observed in three-dimensional fracture propagation, in which robust automatic mesh generation, more general element shapes, and the numerical simulation of highly complex components are essential, and many weeks of human intervention are required to produce an adequate grid. In practical engineering applications, an automatic mesh generator that is capable of achieving conforming boundary recovery and the required element sizegradation is indispensable [1].

Special and continuous attention has been focused on eliminating human effort in the meshing phase and developing more general elements. Automatic mesh generation remains an active field of research. Refs. [2–6] presented overviews of recent activity in solid mechanics and engineering applications. At this stage, truly automatic and robust meshing of arbitrary three-dimensional domains is an attainable goal. The improvement of element shapes has not yet been achieved. New

numerical methods have been developed to circumvent the restrictions in the element shapes of finite element meshes [7–13]; the scaled boundary FEM (SBFEM) is a representative technique.

The SBFEM is a semi-analytical method that was first proposed by Song and Wolf [14,15]. The method was initially developed for modelling wave propagation in unbounded domains and was subsequently used to analyse problems with stress singularities. A considerable amount of effort has been devoted to extending its applications over the past few years. For example, Man [16] simulated plate bending, Lin et al. [17] conducted a sloshing analysis of liquid storage tanks, Goswami [18], Hell [19], and Saputra et al. [20] conducted three-dimensional crack analyses using the SBFEM, and Birk et al. [21] modelled dynamic soil-structure interactions in layered soil using a modified SBFEM. Electrostatic problems [22,23] combined with isogeometric analysis [24], the evaluation of hydrodynamic pressures in the seismic analysis of a Concrete Faced Rockfill Dam [25], and nonlinear analyses of complex plane geometries [26] and short-crested wave interactions [27] have also been performed. Because discretization is only performed on the boundary surface, the SBFEM provides high flexibility in three-dimensional mesh generation, where the shape of a subdomain can be treated as a polyhedron with an arbitrary number of faces. More recently, Liu et al. [7] and Saputra et al. [8] developed an automatic polyhedral mesh generation and scaled boundary finite element analysis.

The discussion presented above is a brief literature review of various applications of the SBFEM to engineering in statics and dynamics. Unfortunately, all of the aforementioned applications were conducted

* Corresponding author at: The State Key Laboratory of Coastal and Offshore Engineering, Dalian University of Technology, Dalian, Liaoning 116024, China.
 E-mail address: zoudegao@dlut.edu.cn (D. Zou).

<https://doi.org/10.1016/j.compgeo.2017.10.021>

Received 25 July 2017; Received in revised form 11 October 2017; Accepted 31 October 2017
 0266-352X/ © 2017 Elsevier Ltd. All rights reserved.

in elastic fields, and none involved nonlinearity. Material nonlinearity is a vital component that must be considered to obtain a reasonable solution in many engineering structure analyses, particularly for the simulation of geotechnical engineering structures, in which nonlinearity is ubiquitous. Accounting for such nonlinearity is the most significant bottleneck in extending the method to other fields.

These limitations of existing methods have led to increasing interest in developing a more versatile SBFEM to eliminate the restrictions on its applications. To the authors' knowledge, the SBFEM has been developed for only simple nonlinear partial differential equations [28], the applications of which are extremely rare. A coupled SBFEM-FEM approach was proposed using the Hilber-Hughes-Taylor- α (HHT- α) technique [29], and soil-structure interaction was modelled while considering elasto-plastic behaviour. More recently, an internal integration technique was presented to replace the original boundary integral scheme. In doing so, Chen et al. [30] provided an alternative method to perform nonlinear analysis using the SBFEM, and the validity of this method was investigated based on the evolution of damage to the Koyna concrete dam.

Although many achievements have been made, several issues remain to be solved. The studies described previously used plane isoparametric elements. Consequently, only triangles or quadrangles can be used as face elements. These element shapes may be sufficient for many applications but cannot be combined seamlessly with many automatic mesh generators, which require polygon faces in a sub-cell. This issue represents another main motivation for the development of more general polyhedral shapes, in which each face can possess an arbitrary number of vertexes in a sub-domain.

The main objective of this paper is to present a robust, automatic, simple and general approach for elasto-plastic rapid design and analysis by combining two highly complementary techniques: the fully automatic octree generator for discretization and the modified nonlinear polyhedron SBFEM (NPSBFEM) for stress analysis. In the first step, an octree polyhedral grid can be readily acquired using an automatic mesh generator. In the second step, a distinctive SBFEM is explored by improving the interpolation function for boundary face elements and the integral strategy for nonlinear simulation.

Polygonal shape functions have reached maturity [31–35], which provides a valuable opportunity to improve the displacement function of the SBFEM. Here, a mean-value approach is incorporated into the method because it is convenient to formulate and program and is general for arbitrary geometries. In this paper, the functions and corresponding gradients are pre-calculated and imported as constants, which can reduce the computational cost of the main program considerably.

In the original SBFEM, only elastic problem was considered. Recently, Ooi et al. [36] made great contribution in solving 2D nonlinear problem with SBFEM. The primary cause of this limitation is that the Gauss points are distributed on the boundary surface. The relationship between strain and stress is not accurately represented. Therefore, an internal integration is introduced to replace the original boundary integral scheme. Three integral strategies are discussed, including the tetrahedral integration rules and the skill utilized in Ref. [30]. The improved method is adopted for several engineering applications, which are described in detail in Section 4. A more flexible and general NPSBFEM is established, and this NPSBFEM can be seamlessly combined with the automatic octree generator.

The remainder of this paper is organized as follows. First, Section 2 gives a brief theoretical derivation of the mean-value shape function. A brief, descriptive account of octree decomposition is provided in Section 3, and the SBFEM for polyhedron formulation is given in Section 4. Polyhedron formulations for elasto-plastic analysis are derived in Section 5, and the reliability of the procedure is demonstrated using four numerical examples in Section 6. Remarks and conclusions are provided in Section 7.

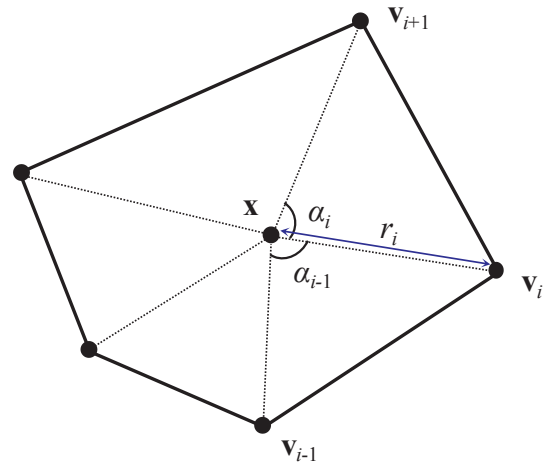


Fig. 1. Mean-value coordinates.

2. Mean-value shape functions on polygons

This section summarizes the mean-value polygonal shape function. Only the key formulations related to the fundamental concept that are necessary for the new technique are presented. A detailed derivation is given in [32–35]. The desirable properties for finite element interpolants discussed in Ref. [35] are satisfied, and the proof is presented.

The mean-value coordinates were first introduced by Floater [33]. For a point \mathbf{x} in the interior of Ω , two primary variables are necessary and are defined as follows: angles $\alpha_i(\mathbf{x}) = \angle \mathbf{xv}_i\mathbf{v}_{i+1}$ and distances $r_i(\mathbf{x}) = \|\mathbf{x} - \mathbf{v}_i\|$, which are illustrated in Fig. 1. Then, for vertex \mathbf{v}_i , a weight function $w_i(\mathbf{x})$ is given by

$$w_i(\mathbf{x}) = \frac{\tan(\alpha_{i-1}/2) + \tan(\alpha_i/2)}{\|\mathbf{x} - \mathbf{v}_i\|} \quad (2-1)$$

$$\tan(\alpha_i/2) = \frac{\sin \alpha_i}{1 + \cos \alpha_i} \quad (2-2)$$

Subsequently, the mean-value coordinates can be expressed as the relative ratio of the weight functions of the different vertices:

$$\lambda_i(\mathbf{x}) = \frac{w_i(\mathbf{x})}{\sum_{j=1}^n w_j(\mathbf{x})} \quad (2-3)$$

where n is the number of vertices. The mean-value shape functions can be readily computed by substituting Eqs. (2-1) and (2-2) into (2-3). Notably, the formulation is still applicable to a non-convex polygon.

Typically, the mean-value shape functions are derived in the physical global coordinates. To couple these functions with the SBFEM and simplify the integration, a technique to construct conforming approximations of polygons is described using mean-value shape functions. Similar to isoparametric elements, the shape function is defined on a canonical element with local coordinates $\xi = (\xi_1, \xi_2) \in \mathbf{R}_0$. Canonical elements are given for a triangle, quadrangle, pentagon and hexagon and are illustrated in Fig. 2. The nodes lie on the same circumcircle in each case, and the geometric centre is located in the centre of the circumcircle; hence, all of the vertices of the polygon are natural neighbours of any point in \mathbf{R}_0 . The vertical coordinates of an n -gon are expressed as $(\cos 2\pi/n, \sin 2\pi/n)$, $(\cos 4\pi/n, \sin 4\pi/n)$, ..., and $(1, 0)$. The shape function can then be defined using the reference coordinate system. Subsequently, each arbitrary polygon can be transformed into corresponding canonical elements using the isoparametric mapping function λ . The mapping for a pentagonal element is illustrated in Fig. 3.

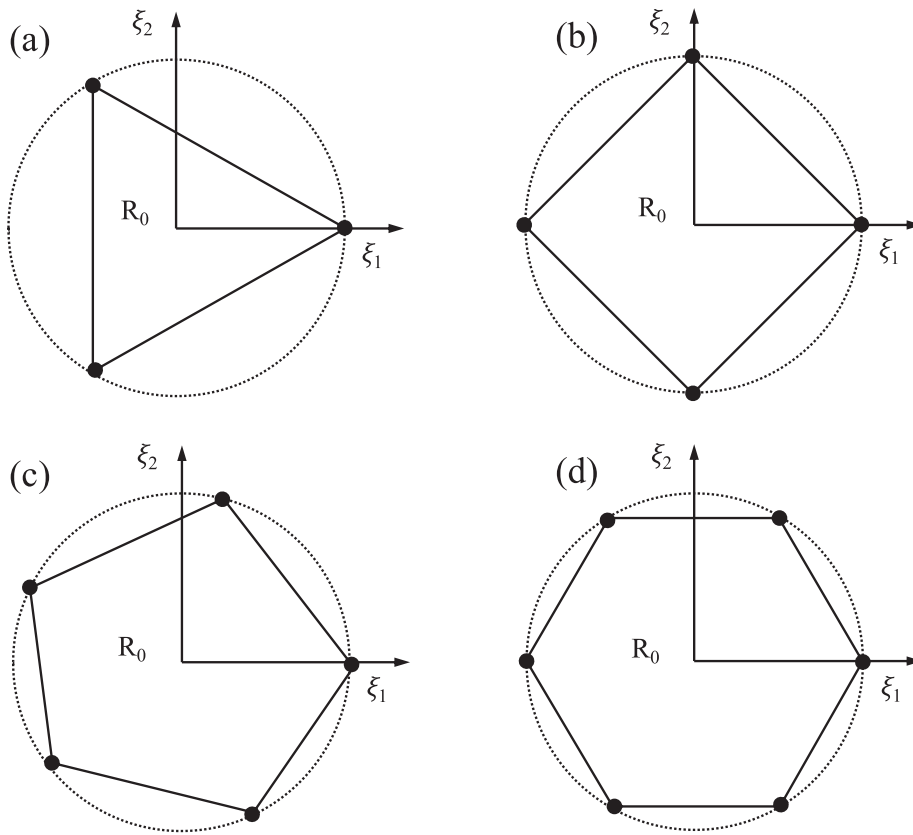


Fig. 2. Canonical elements: (a) triangle, (b) quadrangle, (c) pentagon, and (d) hexagon.

3. Octree decomposition

Octree is a hierarchical data structure that describes how the objects in a scene are distributed using the 3D space occupied by the scene. Spatial decomposition methods based on octree structures were originally presented for use as approximate representations of geometric objects [37]. A cube is typically adopted to enclose the object, which is also called the root. This parallelepiped is subdivided into its eight octants, which are then recursively subdivided several times based on criteria defined by the application. The emergence of the finite octree approach led to an important advancement in the generation of a mesh of a complex three-dimensional model, which resulted in the development of many rapid, efficient and automatic mesh generators [38–41]. This subdivision can achieve any desired level of accuracy. A representative octree grid with three levels is shown in Fig. 4.

The generation of a high-quality octree mesh typically involves several primary procedures, including splitting an edge, trimming a face, trimming a cell and trimming with the recovery of sharp features. A detailed description is provided in Refs. [7,8]. The octree grid is generated automatically by a powerful generator, which reduces the

required human effort considerably.

4. Summary of the scaled boundary finite element method using a polyhedral mesh

The SBFEM inherits the advantage of the boundary element method (BEM); namely, discretization is only conducted on the boundary and does not require a fundamental solution. This method is inherently appropriate for modelling polyhedrons with an arbitrary number of faces and has other promising capabilities. With such an important advantage, the SBFEM is more applicable to complex geometries than other methods. This section provides a summary of the SBFEM in three-dimensional space, and only the equations that are essential for the implementation are provided. A detailed derivation and explanations of these equations are provided in [15,21].

4.1. Polyhedral cells in the modified SBFEM

In the original method, a polyhedral cell can be treated as a subelement in the SBFEM. The boundary is discretized by a combination of

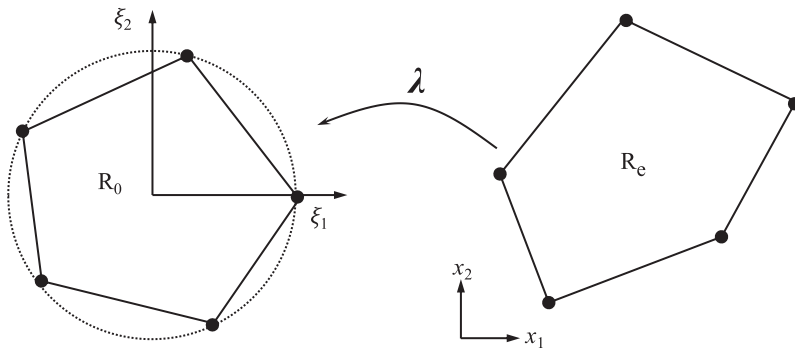


Fig. 3. Isoparametric mapping.

Fig. 4. Octree meshing with three levels.

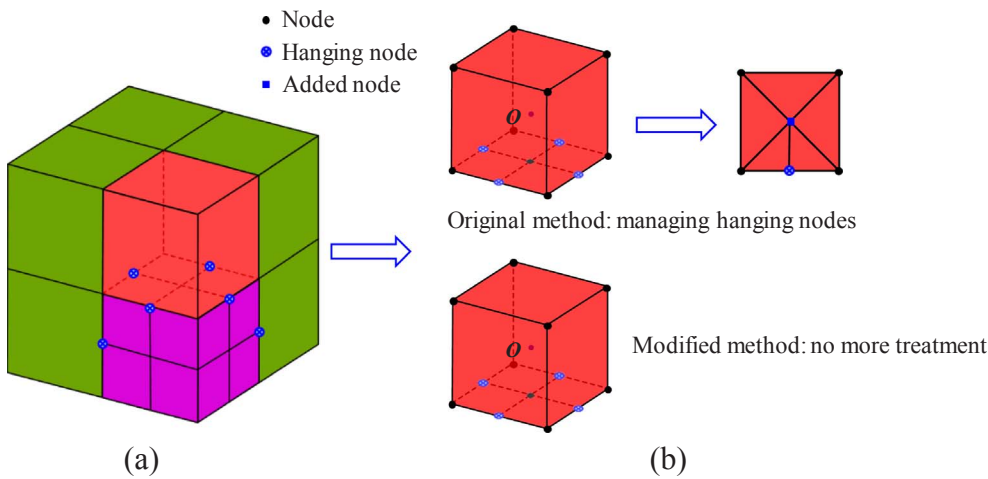
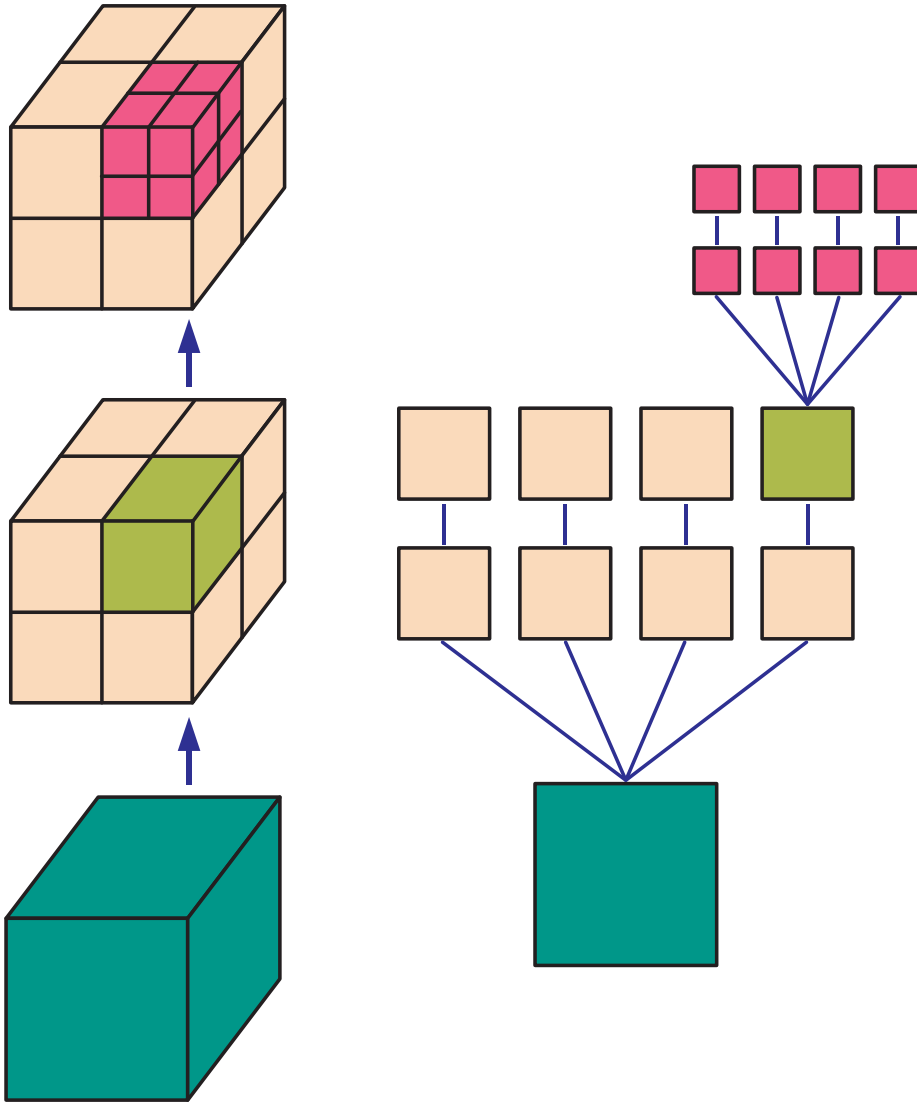


Fig. 5. (a) Balanced octree decomposition with hanging nodes, (b) comparison of the treatments of hanging nodes.

triangular and quadrilateral face elements (see Fig. 5). A so-called scaling centre located inside the subdomain is introduced (Fig. 5), which must be directly visible from the entire sub-element boundary. Here, the geometric centre is selected in each sub-element.

In this paper, the SBFEM has been modified to have access to more

general boundary elements, such as triangles, quadrangles, pentagons, hexagons, and heptagons. Octree sub-elements are illustrated in Fig. 5(b). The hanging nodes have no management requirement. The novel method also allows more diverse shapes, as shown in Fig. 6.

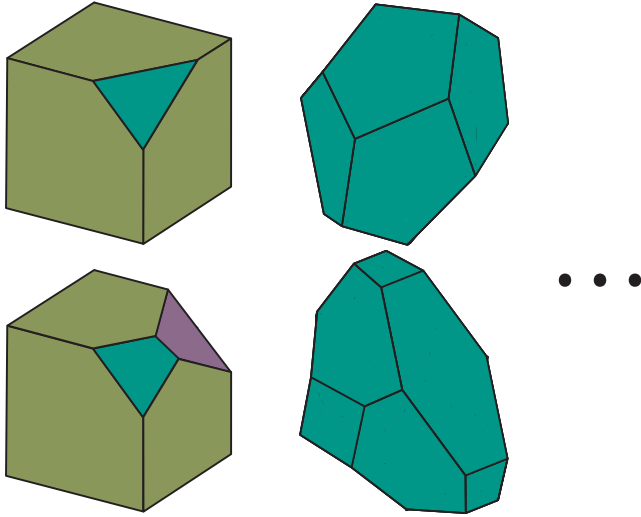


Fig. 6. Representative general sub-element shapes.

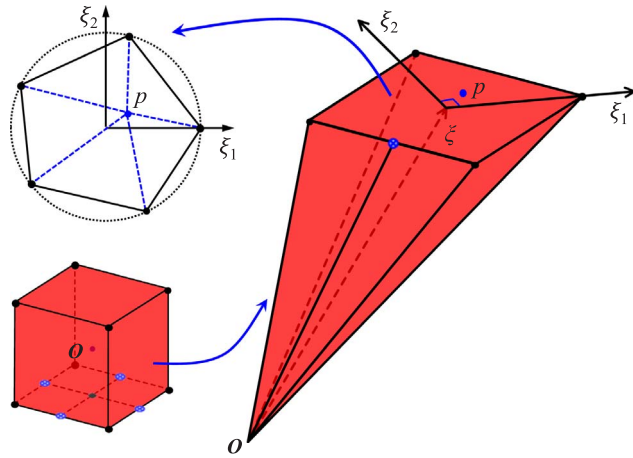


Fig. 7. Modified SBFEM coordinates and isoparametric mapping.

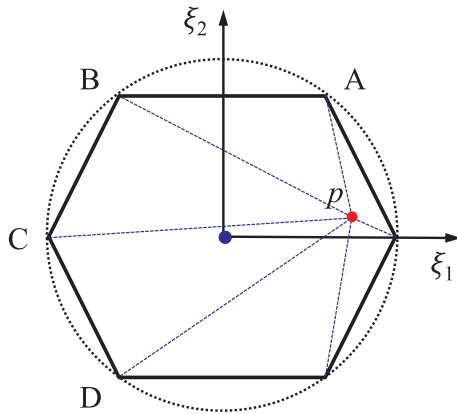


Fig. 8. Mean-value coordinates at point p.

Table 1
Value of the mean-value shape function at point p (4-digit precision).

Vertex	A	B	C	D	E	F
λ_i	0.2201	0.0268	0.0194	0.0221	0.0575	0.6547

4.2. Key equations for the modified polyhedron SBFEM

After the discretization is achieved, the surface elements are constructed using polygonal mean-value shape functions. Similar to the FEM, the concept of isoparametric mapping is used in this study. A pentagonal element is shown as an example in Fig. 7.

For each face element, the domain is interpolated using the polygonal mean-value shape function λ formulated with local coordinates (ξ_1, ξ_2) as discussed in Section 2, where (ξ_1, ξ_2) are the scaled boundary coordinates. Then, a point (x, y, z) on the boundary can be written as

$$x(\xi_1, \xi_2) = \lambda(\xi_1, \xi_2)xy(\xi_1, \xi_2) = \lambda(\xi_1, \xi_2)yz(\xi_1, \xi_2) = \lambda(\xi_1, \xi_2)z \quad (4-1)$$

where x, y, z is the coordinate vector belonging to the boundary face elements. A dimensionless radial coordinate ξ is introduced, which connects the scaling centre $O(\hat{x}_0, \hat{y}_0, \hat{z}_0)$ and the boundary nodes. Therefore, in the SBFEM coordinates (ξ, ξ_1, ξ_2) , an arbitrary point $(\hat{x}, \hat{y}, \hat{z})$ inside the domain can be expressed as

$$\begin{aligned} \hat{x}(\xi, \xi_1, \xi_2) &= \xi\lambda(\xi_1, \xi_2)x + \hat{x}_0\hat{y}(\xi, \xi_1, \xi_2) = \xi\lambda(\xi_1, \xi_2)y + \hat{y}_0\hat{z}(\xi, \xi_1, \xi_2) \\ &= \xi\lambda(\xi_1, \xi_2)z + \hat{z}_0 \end{aligned} \quad (4-2)$$

Similar to the FEM, the isoparametric mapping technique is adopted, in which a transformational matrix is needed, as expressed in Eq. (4-3)

$$J_m(\xi_1, \xi_2) = \begin{bmatrix} x(\xi_1, \xi_2) & y(\xi_1, \xi_2) & z(\xi_1, \xi_2) \\ x(\xi_1, \xi_2)_{\xi_1} & y(\xi_1, \xi_2)_{\xi_1} & z(\xi_1, \xi_2)_{\xi_1} \\ x(\xi_1, \xi_2)_{\xi_2} & y(\xi_1, \xi_2)_{\xi_2} & z(\xi_1, \xi_2)_{\xi_2} \end{bmatrix} \quad (4-3a)$$

$$|J_m(\xi_1, \xi_2)| = x(y_{\xi_1}z_{\xi_2} - z_{\xi_1}y_{\xi_2}) + y(z_{\xi_1}x_{\xi_2} - x_{\xi_1}z_{\xi_2}) + z(x_{\xi_1}y_{\xi_2} - y_{\xi_1}x_{\xi_2}) \quad (4-3b)$$

The derivatives can be extracted as follows:

$$x(\xi_1, \xi_2)_{\xi_1} = \lambda(\xi_1, \xi_2)_{\xi_1}xy(\xi_1, \xi_2)_{\xi_1} = \lambda(\xi_1, \xi_2)_{\xi_1}yz(\xi_1, \xi_2)_{\xi_1} = \lambda(\xi_1, \xi_2)_{\xi_1}z \quad (4-4a)$$

$$x(\xi_1, \xi_2)_{\xi_2} = \lambda(\xi_1, \xi_2)_{\xi_2}xy(\xi_1, \xi_2)_{\xi_2} = \lambda(\xi_1, \xi_2)_{\xi_2}yz(\xi_1, \xi_2)_{\xi_2} = \lambda(\xi_1, \xi_2)_{\xi_2}z \quad (4-4b)$$

In this manner, a new matrix LDu can be established to represent the gradient of the shape function with respect to the local coordinates, as given in Eqs. (4) and (5).

$$LDu = \begin{bmatrix} \lambda(\xi_1, \xi_2) \\ \lambda(\xi_1, \xi_2)_{\xi_1} \\ \lambda(\xi_1, \xi_2)_{\xi_2} \end{bmatrix} \quad (4-5)$$

For three-dimensional problems, the displacement components at a point (ξ, ξ_1, ξ_2) inside a pyramid are interpolated using a presumptive radial displacement function $u(\xi)$ and a mean-value shape function, which is written as Eq. (4-6), where $[I]$ is the 3×3 identity matrix, and λ_i ($i = 1, 2, 3 \dots n$) is the nodal interpolated function defined in a canonical isoparametric element. The expression of the polygonal shape function is extremely complex; thus, the description is not expanded here.

$$u(\xi, \xi_1, \xi_2) = \lambda^u(\xi_1, \xi_2)u(\xi) \quad (4-6a)$$

$$\lambda^u(\xi_1, \xi_2) = [\lambda_1[I], \lambda_2[I], \lambda_3[I], \lambda_4[I] \dots] \quad (4-6b)$$

4.3. Polyhedral shape functions based on the SBFEM

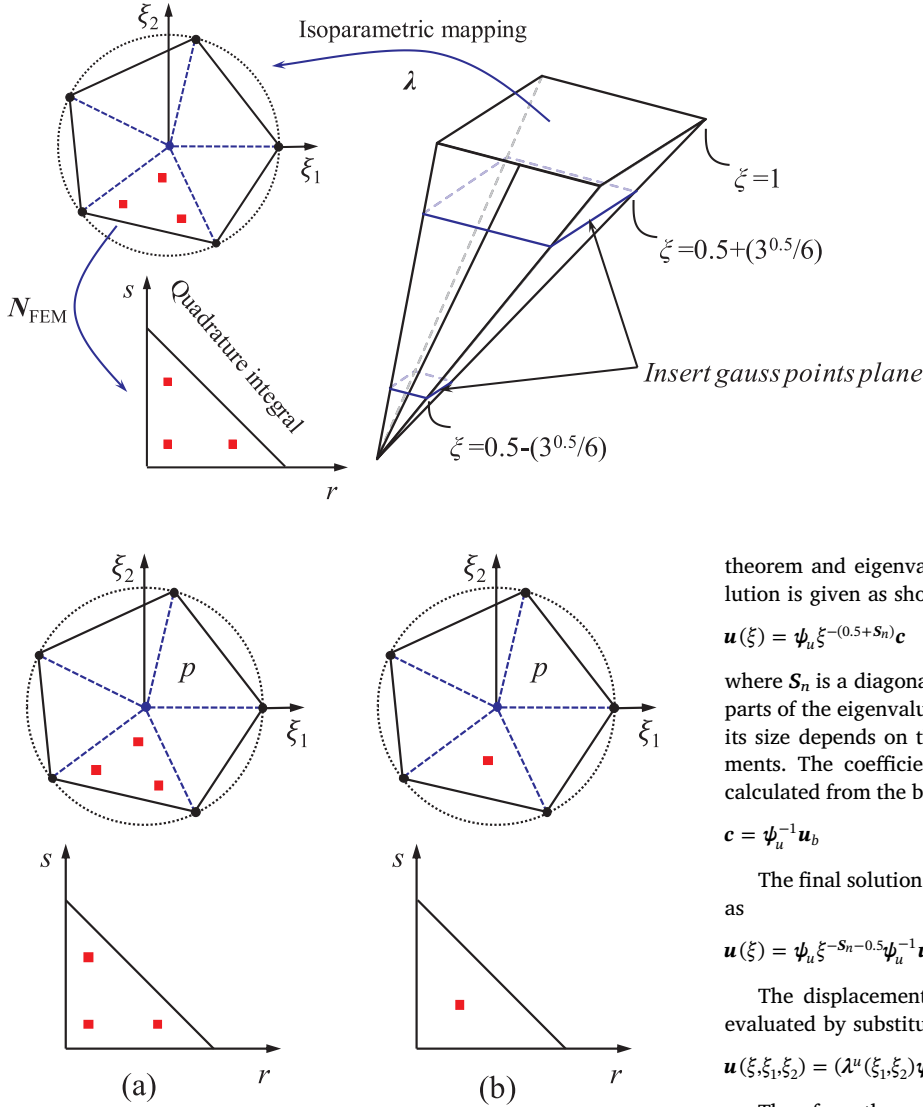
To obtain the assumed radial function $u(\xi)$, an equilibrium equation can be extracted using the mechanical equilibrium condition as follows:

$$E_0\xi^2u(\xi)_{\xi\xi} + (2E_0 + E_1^T - E_1)\xi u(\xi)_{\xi} + (E_1^T - E_2)u(\xi) + F(\xi) = 0 \quad (4-7)$$

where the coefficient matrices E_0, E_1 , and E_2 are intermediate variables

Table 2Value of the derivatives at point p (4-digit precision).

Vertex		A	B	C	D	E	F
LDu	λ_i	0.2201	0.0268	0.0194	0.0221	0.0575	0.6547
	$\partial\lambda_i/\partial\xi_1$	-0.3006	-0.1675	-0.1161	-0.1322	-0.3358	1.0522
	$\partial\lambda_i/\partial\xi_2$	0.8177	-0.0442	-0.0448	-0.0625	-0.3187	-0.3476

**Fig. 10.** Comparison of the distributions of Gauss points in each sub-triangle: (a) Scheme 1 and (b) Scheme 2.

that depend only on the geometry and material properties of the domain and are evaluated on the face elements and assembled over the discretized polyhedron boundary. These coefficient matrices can be calculated as follows:

$$E_0 = \int_{-1}^{+1} \int_{-1}^{+1} \mathbf{B}_1^T \mathbf{D} \mathbf{B}_1 |J_m| d\xi_1 d\xi_2 \quad (4-8a)$$

$$E_1 = \int_{-1}^{+1} \int_{-1}^{+1} \mathbf{B}_2^T \mathbf{D} \mathbf{B}_1 |J_m| d\xi_1 d\xi_2 \quad (4-8b)$$

$$E_2 = \int_{-1}^{+1} \int_{-1}^{+1} \mathbf{B}_2^T \mathbf{D} \mathbf{B}_2 |J_m| d\xi_1 d\xi_2 \quad (4-8c)$$

where \mathbf{B}_1 and \mathbf{B}_2 are transition matrices, \mathbf{D} is a constitutive matrix, and λ is the polygonal shape function for a surface element.

The equilibrium equation can be solved using the mathematical

Fig. 9. Distribution of Gauss points for Scheme 1.

theorem and eigenvalue decomposition technique. Ultimately, the solution is given as shown in Eq. (4-9)

$$\mathbf{u}(\xi) = \psi_u \xi^{-(0.5+S_n)} \mathbf{c} \quad (4-9)$$

where S_n is a diagonal matrix, and the entries are composed of the real parts of the eigenvalues. The matrix ψ_u is the modal displacements, and its size depends on the degrees of freedom (DOFs) of the surface elements. The coefficient \mathbf{c} is the integration constants, which can be calculated from the boundary nodal displacement vector $\mathbf{u}_b = \mathbf{u}(\xi = 1)$.

$$\mathbf{c} = \psi_u^{-1} \mathbf{u}_b \quad (4-10)$$

The final solutions for the radial displacements $\mathbf{u}(\xi)$ can be obtained as

$$\mathbf{u}(\xi) = \psi_u \xi^{-S_n-0.5} \psi_u^{-1} \mathbf{u}_b \quad (4-11)$$

The displacement field $\mathbf{u}(\xi, \xi_1, \xi_2)$ for the polyhedral element is evaluated by substituting Eq. (4-11) into Eq. (4-6a).

$$\mathbf{u}(\xi, \xi_1, \xi_2) = (\lambda^u(\xi_1, \xi_2) \psi_u \xi^{-(0.5+S_n)} \psi_u^{-1}) \mathbf{u}_b \quad (4-12)$$

Therefore, the polyhedral element shape function $\Phi(\xi, \xi_1, \xi_2)$ formulated based on the SBFEM is extracted as

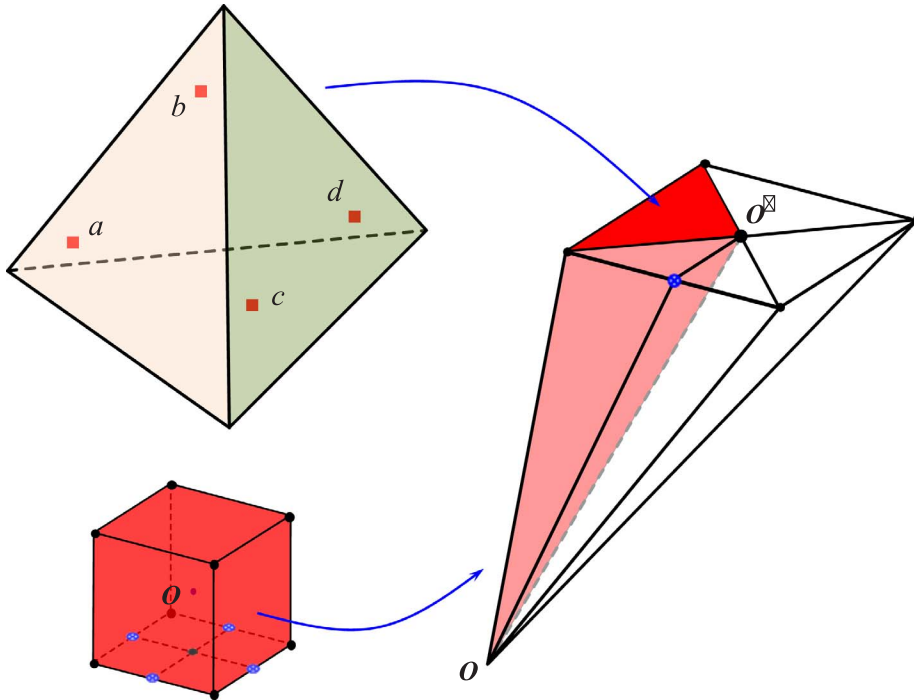
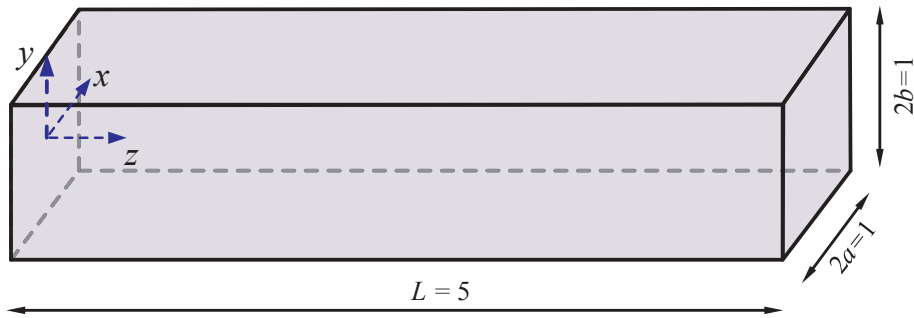
$$\Phi(\xi, \xi_1, \xi_2) = \lambda^u(\xi_1, \xi_2) \psi_u \xi^{-(0.5+S_n)} \psi_u^{-1} \quad (4-13)$$

The polyhedral element shape functions can be readily computed once the polygonal shape function for the boundary elements is known. The values of these shape functions and the matching derivatives are required.

In this paper, the values of the functions λ and the corresponding derivatives \mathbf{LDu} were pre-calculated using an external MATLAB code, which significantly simplified the expression of the polyhedral element shape functions $\Phi(\xi, \xi_1, \xi_2)$ as well as the coefficient matrix used in the SBFEM. Therefore, the presented polyhedral element does not require a complex integration scheme, which is a significant advantage.

Here, information about the shape function and the derivatives \mathbf{LDu} is discussed to provide the reader with a general understanding. A convex six-node canonical element with the nodal coordinates (4-digit precision) (0.5, 0.8660), (-0.5, 0.8660), (-1.0, 0.0), (-0.5,

Fig. 11. Distribution of Gauss points in each sub-tetrahedron.

Fig. 12. Shear-loaded beam of length L with a rectangular cross-section of width $2a$ and height $2b$.

-0.8660), $(0.5, -0.8660)$ and $(1, 0)$ is adopted as an example. The mean value coordinates are evaluated at point p with the coordinates $(0.75, 0.1443)$. Then, the domain is triangulated with p as an internal point, which is shown in Fig. 8. The polygonal shape functions and derivatives can be computed by substituting these known variables, and the results are listed in Tables 1 and 2.

4.4. Strain and stress fields

The radial analytical displacement function $u(\xi)$ can be obtained after the derivation provided above. Using the strain field formulation provided by Wolf [14], the strain field of a polyhedron can be rewritten by substituting in Eq. (4-11) as follows:

$$\varepsilon(\xi, \xi_1, \xi_2) = (\mathbf{B}_1(\xi_1, \xi_2)\psi_u(-S_n - 0.5)\xi^{-(1.5+S_n)}\psi_u^{-1})\mathbf{u}_b + \left(\frac{1}{\xi}\mathbf{B}_2(\xi_1, \xi_2)\psi_u\xi^{-(0.5+S_n)}\psi_u^{-1}\right)\mathbf{u}_b \quad (4-14)$$

By extracting the coefficient before \mathbf{u}_b , the strain fields of the scaled boundary finite element can be simplified as

$$\varepsilon(\xi, \xi_1, \xi_2) = \mathbf{B}(\xi, \xi_1, \xi_2)\mathbf{u}_b \quad (4-15a)$$

$$\mathbf{B}(\xi, \xi_1, \xi_2) = (\mathbf{B}_1(\xi_1, \xi_2)\psi_u(-S_n - 0.5)\xi^{-(1.5+S_n)}\psi_u^{-1}) + \left(\frac{1}{\xi}\mathbf{B}_2(\xi_1, \xi_2)\psi_u\xi^{-(0.5+S_n)}\psi_u^{-1}\right) \quad (4-15b)$$

where $\mathbf{B}(\xi, \xi_1, \xi_2)$ is the strain-displacement matrix of the polyhedral element.

In elasto-plastic analysis, the incremental strain field can be decomposed into incremental elastic and plastic strain components. The plastic strain increment can then be determined from the plastic flow rule. Assuming associative plasticity and using the yield functions F and plastic multiplier $\Delta\lambda$, the plastic strain increment is formulated as

$$\Delta\varepsilon = \Delta\varepsilon_e + \Delta\varepsilon_p \Delta\varepsilon_p = \frac{\partial F}{\partial \sigma} \Delta\lambda \quad (4-16)$$

where $F = F(\sigma, \kappa)$ is defined as the yield function in the formulation and is determined from the current stress state σ and the hardening parameter κ . Using Hooke's law, the incremental stress field $\Delta\sigma$ can be written as

$$\Delta\sigma = \mathbf{D}_{ep} \Delta\varepsilon \quad (4-17)$$

where \mathbf{D}_{ep} is the elasto-plastic constitutive matrix. Substituting Eq. (4-15a) into the formulation for the incremental strain field $\Delta\varepsilon$, the incremental stress field is expressed as

$$\Delta\sigma(\xi, \xi_1, \xi_2) = \mathbf{D}_{ep} \mathbf{B}(\xi, \xi_1, \xi_2) \Delta\mathbf{u}_b \quad (4-18)$$

where $\Delta\mathbf{u}_b$ is the nodal displacement increment on the boundary surface.

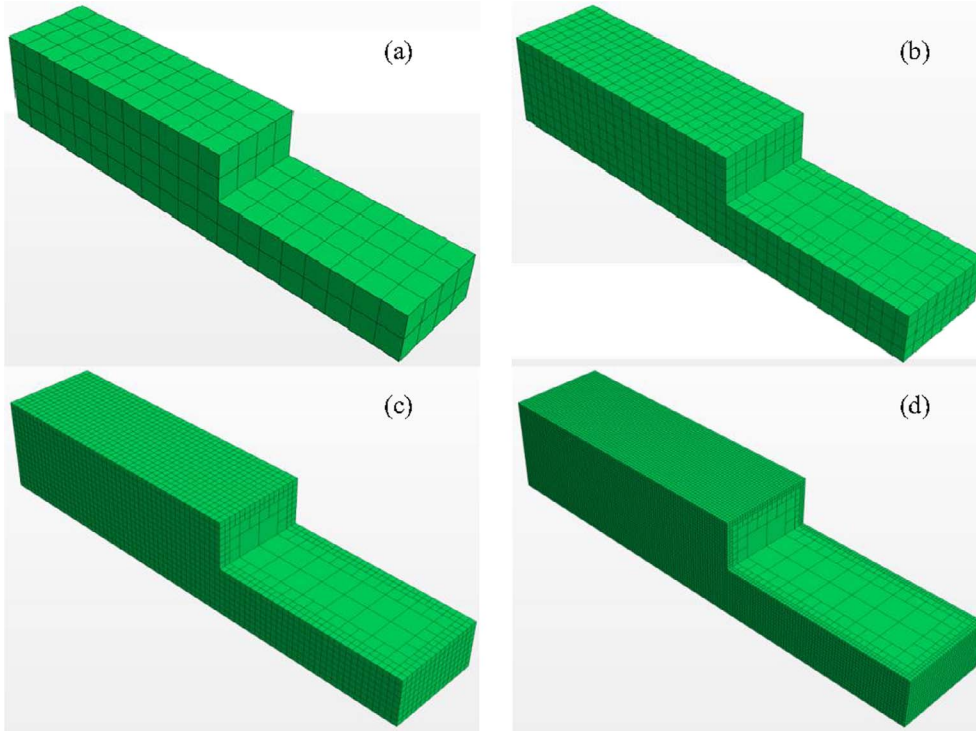


Fig. 13. Clipped views of the four levels of mesh refinement.

Table 3
Elements and nodes of the four meshes.

Mesh	Elements	Nodes
Mesh (a)	320	525
Mesh (b)	2056	3023
Mesh (c)	10,400	14,961
Mesh (d)	46,744	66,899

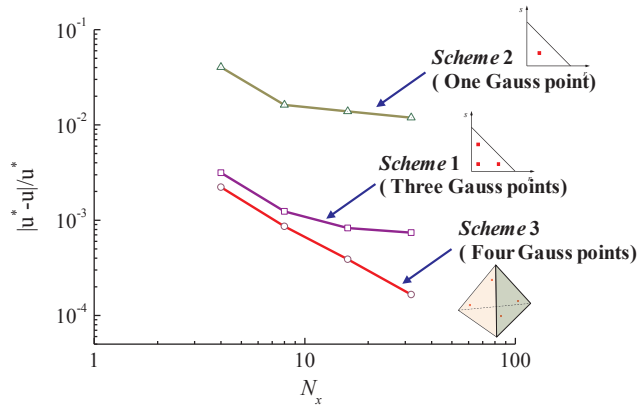


Fig. 14. Displacement error as a function of the mesh density along the beam, N_x , for the boundary value problem of a cantilever beam subjected to an end-shear load.

5. Polyhedron formulation for elasto-plastic analysis

In this section, the necessary formulations for the new technique are given, and the elasto-plastic derivation of polyhedral elements based on the SBFEM is provided. Similar to the FEM, the scaled boundary polyhedron formulation for elasto-plasticity is performed using the principle of virtual work, which is written in SBFEM coordinates as

$$\int_{\Omega} \delta \varepsilon^T \Delta \sigma(\xi, \xi_1, \xi_2) d\Omega = \int_{\Gamma} \delta u^T f_t d\Gamma + \int_{\Gamma} \delta u^T f_b d\Gamma - \int_{\Omega} \delta \varepsilon^T \sigma(\xi, \xi_1, \xi_2) d\Omega \quad (5-1)$$

where $\Delta \sigma(\xi, \xi_1, \xi_2)$ is the incremental stress field, f_t and f_b are the surface traction and body force intensity, respectively, and $\delta \varepsilon(\xi, \xi_1, \xi_2)$ is the virtual strain field corresponding to the virtual displacement field $\delta u(\xi, \xi_1, \xi_2)$. By substituting the equations for these variables from the previous sections, the expanded formulation of Eq. (5-1) can be expressed as

$$\left(\int_{\Omega} B^T(\xi, \xi_1, \xi_2) D_{ep} B(\xi, \xi_1, \xi_2) d\Omega \right) \Delta u_b = \left(\int_{\Gamma} \Phi^T(\xi, \xi_1, \xi_2) f_t d\Gamma + \int_{\Gamma} \Phi^T(\xi, \xi_1, \xi_2) f_b d\Gamma \right) - \left(\int_{\Omega} B^T(\xi, \xi_1, \xi_2) \sigma(\xi, \xi_1, \xi_2) d\Omega \right) \quad (5-2)$$

where D_{ep} is the elasto-plastic constitutive matrix obtained from the constitutive model. The term within the first set of parentheses on the left-hand side of Eq. (5-2) is the elasto-plastic stiffness matrix K_{ep} , the second term is the external load vector R_{ext} , and the last term is the internal load vector R_{int} . Thus, Eq. (5-2) can be simplified as

$$K_{ep} \Delta u_b = R_{ext} - R_{int} \quad (5-3)$$

Eq. (5-3) is a system of nonlinear equilibrium equations, which can be assembled element-by-element. The equilibrium equation of the problem domain is defined as

$$\left(\sum_{i=1}^{nPol} K_{ep} \right) \Delta U_b = \sum_{i=1}^{nPol} (R_{ext} - R_{int}) \quad (5-4)$$

where ΔU_b is the incremental nodal displacement vector on the boundary of the entire domain. Standard nonlinear iterative procedures, such as modified Newton-Raphson iterations, can be used to solve this equation.

5.1. Integral Gauss point strategies

Three integral strategies are introduced in this section. The distribution and weight of the Gauss points are given. To simplify the nomenclature, the methods are referred to as Schemes 1, 2, and 3. Detailed descriptions are provided below.

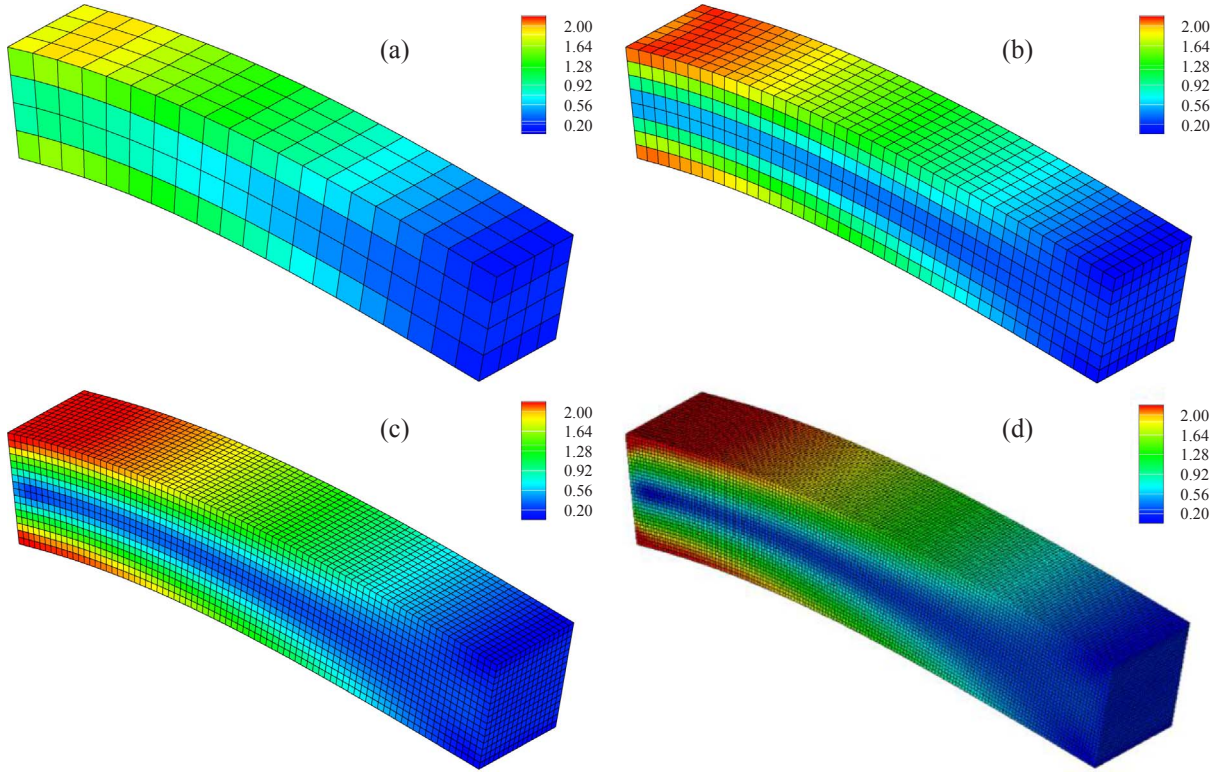


Fig. 15. Von Mises stress fields from the Scheme 3 solutions of the boundary value problem of a cantilever beam subjected to an end-shear load.

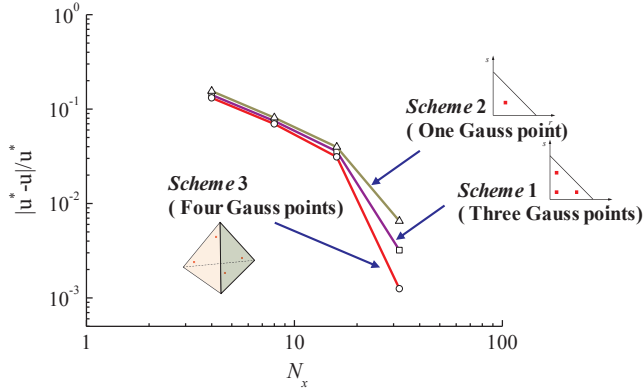


Fig. 16. Displacement error as a function of the mesh density along the beam N_x for the boundary value problem of a cantilever beam subjected to pure torsion.

5.1.1. Scheme 1

A new numerical integration scheme is needed when the plane elements contain more than 4 sides. Here, the canonical elements are sub-divided into triangles, and the standard quadrature rules are used on each triangle to determine the solution. The divided sub-triangles are used solely for numerical integration. A diagram of the process is shown in Fig. 9, where λ is the mean-value polygonal shape function, and N_{FEM} is the linear triangular shape function, as in the FEM. A detailed introduction to the entire process is provided below.

First, each boundary element is transferred to the matching canonical element (see Fig. 2). Next, each element is sub-divided into triangles, and three integral points are selected in each sub-triangle. The rule of the selection is identical to that in the FEM, where the coordinates (r, s) of the three points are determined as $(1/6, 1/6)$, $(2/3, 1/6)$, and $(1/6, 2/3)$, and the weights of all points are $1/3$. The points distributed on the boundary are called surface Gauss points.

Subsequently, for nonlinear applications, systematic internal integral points are introduced as the coordinate ξ varies from zero to one

from the scaling centre to the boundary surface in the radial direction. According to the principle of integration in the one-dimensional element, the values of the points located at $0.5 \times \left(1 \pm \frac{\sqrt{3}}{3}\right)$ can be considered. For this paper, this approach leads to two planes with different ξ values, as shown in Fig. 9. The quadrature points inserted into the two planes are the same as the surface Gauss points, whereas the weights are $1/6$. These points can be referred to as volume Gauss points.

5.1.2. Scheme 2

Scheme 2 is similar to Scheme 1 but has minor differences. The surface Gauss points are consistent with each other; the only difference is the selection of the volume Gauss points. Only one point is adopted in each sub-triangle included in the two specified planes, which means that the order of the integral precision is linear, and the coordinates are $(1/3, 1/3)$. An explanatory drawing is shown in Fig. 10.

5.1.3. Scheme 3

The modified method is different from the traditional polyhedral FEM. The discretization is only performed on the boundary, and the shape functions and gradients for the boundary elements are pre-calculated, which results in a relatively straightforward element shape function and integral functions instead of the original highly complex formulations. Hence, the tetrahedral integration rules would not introduce a computational burden in this method.

For each boundary element, a pyramid can be obtained by dropping segments from the scaling centre to each point of the surface element. The tetrahedral subdivision is then performed using the face centroids (O) and the centroid of the polyhedron (O). Hereafter, standard integration rules for tetrahedrons can be used, and a simple illustration is provided in Fig. 11. Four points are utilized in this study, which are defined as volume coordinates $a(\alpha, \beta, \beta, \beta)$, $b(\beta, \alpha, \beta, \beta)$, $c(\beta, \beta, \alpha, \beta)$ and $d(\beta, \beta, \beta, \alpha)$, where α and β are equal to 0.5854102 and 0.1381966, respectively. The weights for all of the points are $1/24$, as in the FEM.

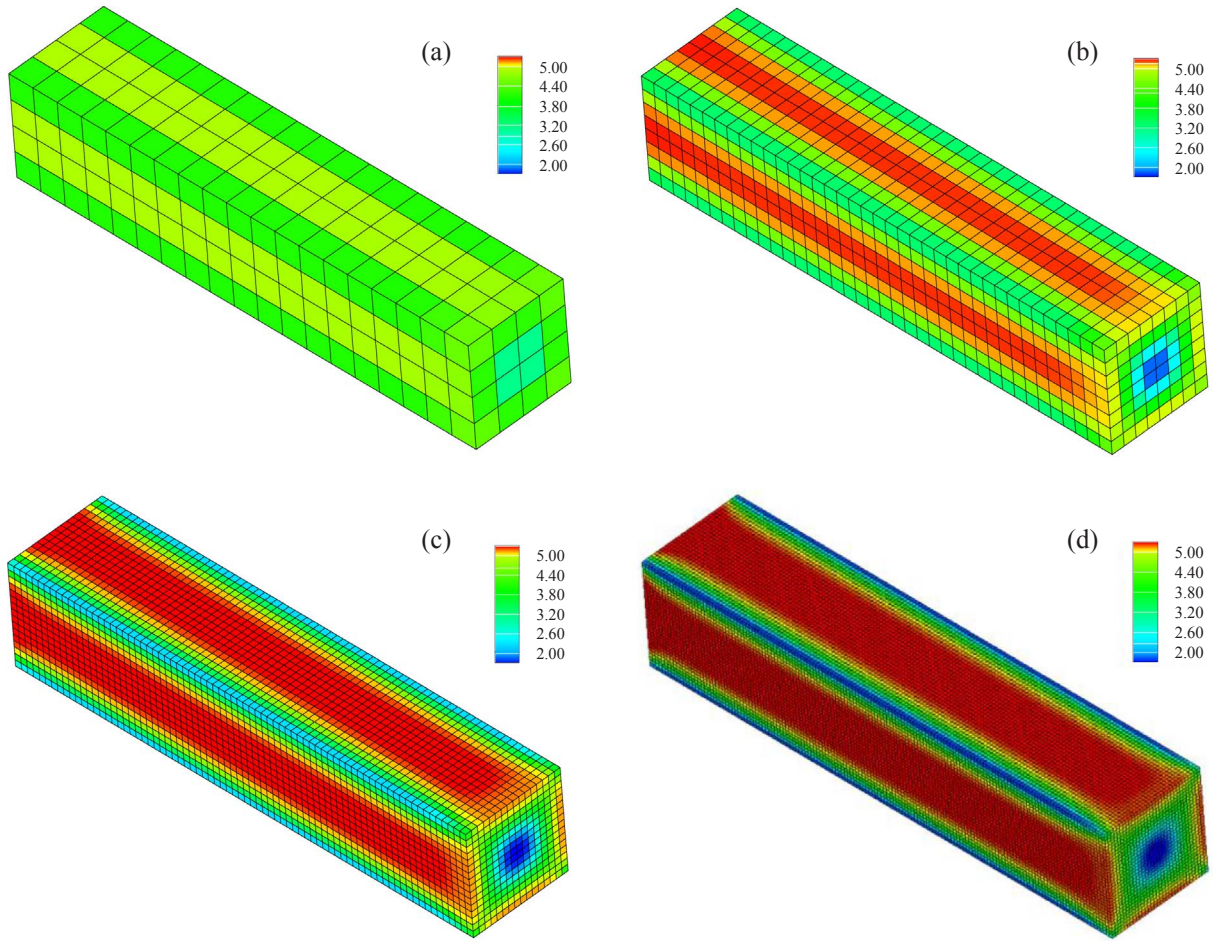


Fig. 17. Von Mises stress fields from the Scheme 3 solutions of the boundary value problem of a cantilever beam subjected to pure torsion.

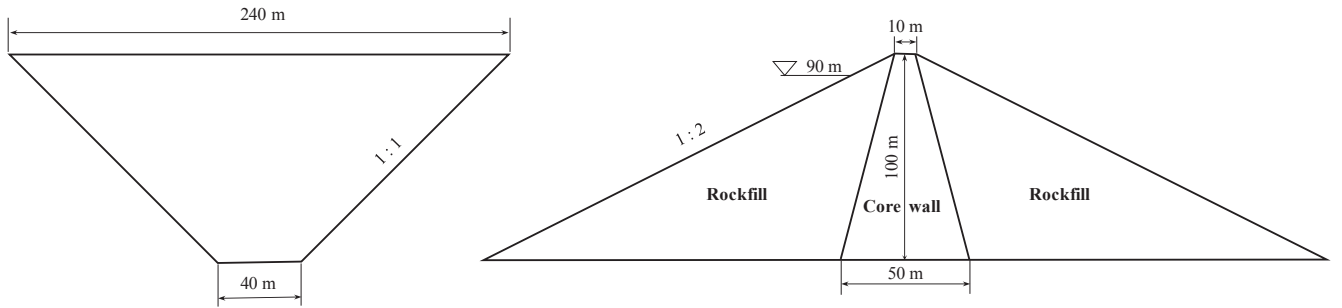


Fig. 18. Geometry and material composition of a typical core wall dam.

5.2. Calculation of the elasto-plastic stiffness matrix

A systematic integral technique is used in the modified method instead of the boundary quadrature. The volume Gauss points discussed in the previous section are employed. A polyhedral formulation of the elasto-plastic stiffness matrix can be extracted from Eqs. (5-2) and (5-3), as shown in Eq. (5-5).

$$\mathbf{K}_{ep} = \int_{\Omega} \mathbf{B}^T(\xi, \xi_1, \xi_2) \mathbf{D}_{ep} \mathbf{B}(\xi, \xi_1, \xi_2) d\Omega \quad (5-5)$$

The value of \mathbf{K}_{ep} of the polyhedron is determined by integrating over each pyramid with the matching quadrature points in the selected plane

$$\mathbf{K}_{ep} = \sum_{i=1}^{m \cdot p_k} \mathbf{B}^i(\xi, \xi_1, \xi_2) \mathbf{D}_{ep}^i \mathbf{B}^i(\xi, \xi_1, \xi_2) V_i \quad (5-6)$$

where m represents the number of surface elements in the polyhedron,

p_k denotes the total number of quadrature points in the k^{th} surface element, $\mathbf{B}^i(\xi, \xi_1, \xi_2)$ represents the strain displacement transformation matrix computed on the i^{th} Gauss point, which can be obtained from Eq. (4-15b), \mathbf{D}_{ep}^i expresses the elasto-plastic constitutive matrix of the i^{th} Gaussian and is calculated from the given plasticity model, and V_i is the volume of the i^{th} point in V_e . The global elasto-plastic stiffness matrix of the solving domain can be evaluated after each \mathbf{K}_{ep} has been computed for the polyhedrons.

5.3. Calculation of the external load vector

The external load vector \mathbf{R}_{ext} can be extracted from Eq. (5-2) and is expressed as

$$\mathbf{R}_{ext} = \int_{\Gamma} \Phi^T(\xi, \xi_1, \xi_2) \mathbf{f}_t d\Gamma + \int_{\Omega} \Phi^T(\xi, \xi_1, \xi_2) \mathbf{f}_b d\Omega \quad (5-7)$$

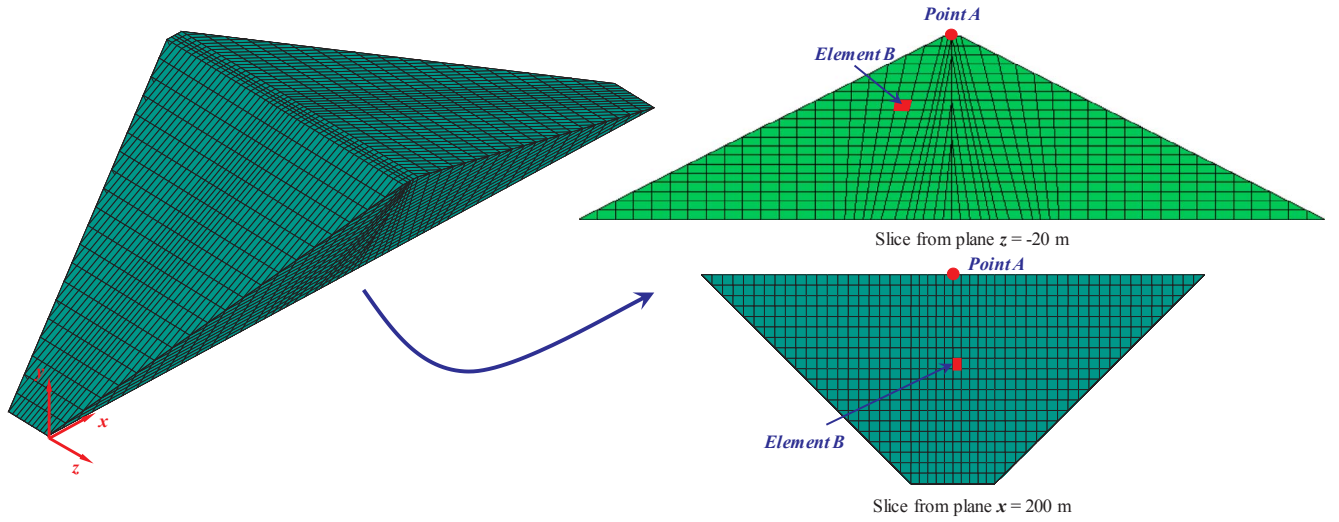


Fig. 19. Traditional mesh of the core wall dam, including two marked points and three elements.

Table 4
Generalized plastic parameters of the core wall.

G_0	K_0	M_g	M_f	α_f	α_g	H_0	H_{U0}	m_s
800	900	1.12	1.12	0.45	0.45	1800	3000	0.5
m_v	m_l	m_u	r_d	γ_{DM}	γ_u	β_0	β_1	
0.5	0.2	0.5	100	50	4	10	0.008	

Table 5
Rockfill material parameters in the modified generalized plasticity model.

G_0	K_0	M_g	M_f	α_f	α_g	H_0	H_{U0}	m_s
1000	1400	1.8	1.38	0.45	0.4	800	1200	0.5
m_v	m_l	m_u	r_d	γ_{DM}	γ_u	β_0	β_1	
0.5	0.2	0.2	180	50	4	35	0.022	

The first term on the right-hand side of Eq. (5-7) is the distributed load on the boundary. It can be further simplified by considering that $(\xi = 1) \Phi(\xi, \xi_1, \xi_2) = \lambda^u(\xi_1, \xi_2)$ applies at the boundary; this can be rewritten as

$$\int_{\Gamma} \Phi^T(\xi, \xi_1, \xi_2) f_t d\Gamma = \int_{-1}^1 \lambda^u(\xi_1, \xi_2) |J(\xi_1, \xi_2)| f_t d\xi_1 d\xi_2 \quad (5-8)$$

The second term is the body load vector. For the case of a constant body load, this term is expressed using numerical integration with the Gauss points

$$\int_{\Omega} \Phi^T(\xi, \xi_1, \xi_2) f_b d\Omega = \sum_{k=1}^m \sum_{i=1}^{p_k} [\lambda_{ki}^u(\xi_1, \xi_2) \psi_u \xi_i^{-(0.5+S_n)} \psi_u^{-1}]^T f_b V_{ki} \quad (5-9)$$

5.4. Calculation of the internal load vector

The formulation of the load vector that results from the internal stresses is defined in Eq. (5-10), which is obtained from Eq. (5-2).

$$\mathbf{R}_{int} = \int_{\Omega} \mathbf{B}^T(\xi, \xi_1, \xi_2) \boldsymbol{\sigma}(\xi, \xi_1, \xi_2) d\Omega \quad (5-10)$$

Here, the Gauss numerical integration is introduced into the summation. First, the strain field $\boldsymbol{\epsilon}(\xi, \xi_1, \xi_2)$ can be calculated from Eq. (4-15a) after the nodal displacements \mathbf{u}_b on the boundary are determined. Next, the stress field $\boldsymbol{\sigma}_i(\xi, \xi_1, \xi_2)$ on each Gauss point is captured by substituting the elasto-plastic constitutive matrix \mathbf{D}_{ep}^i , and the formulation is expressed as

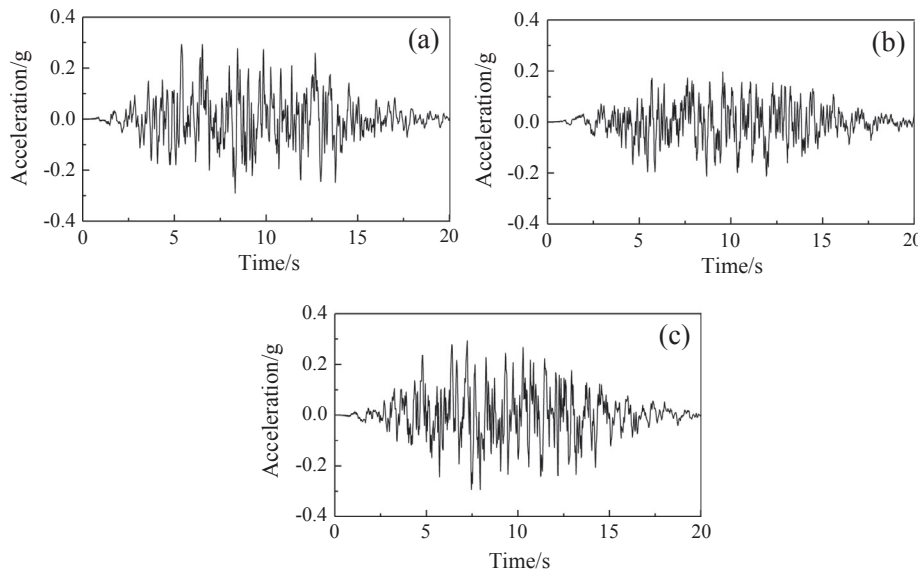


Fig. 20. Input acceleration records: (a) x-direction, (b) y-direction and (c) z-direction.

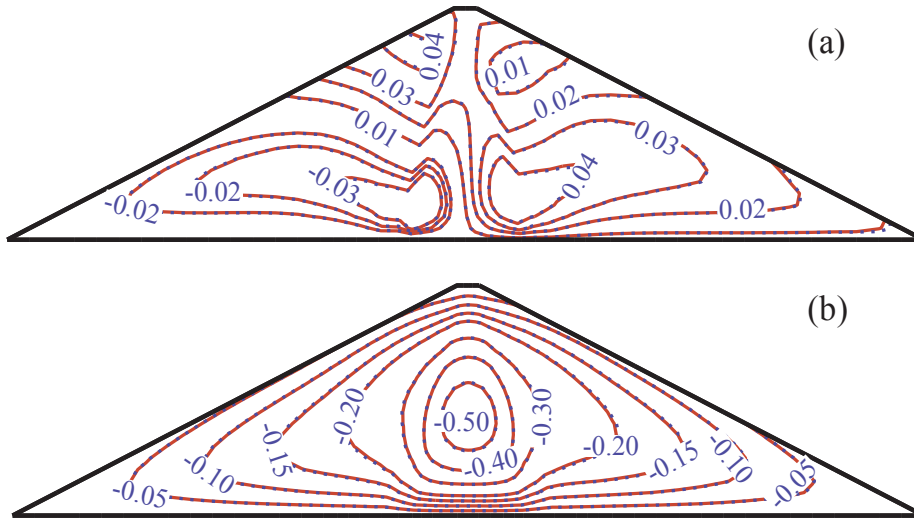


Fig. 21. Displacements of the maximum cross-section after impoundment (units: m): (a) x-direction and (b) y-direction.

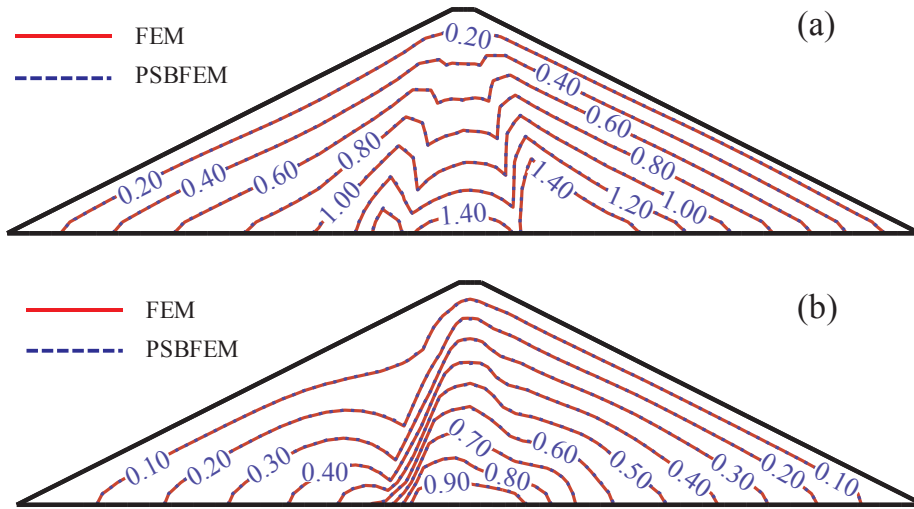


Fig. 22. Principal stresses of the maximum cross-section after impoundment (units: MPa): (a) maximum principal stress and (b) minimum principal stress.

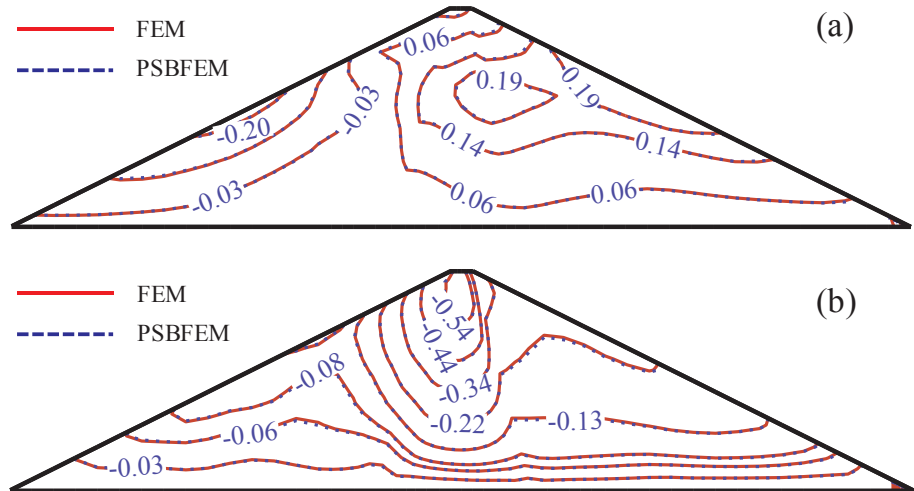


Fig. 23. Displacements of the maximum cross-section after the earthquake ground motion (units: m): (a) x-direction and (b) y-direction.

$$\mathbf{R}_{int} = \sum_{k=1}^m \sum_{i=1}^{p_k} \mathbf{B}^{ki}(\xi, \xi_1, \xi_2)^T \boldsymbol{\sigma}_{ki}(\xi, \xi_1, \xi_2) \mathbf{V}_{ki} \quad (5-11)$$

6. Numerical example

This section presents the numerical simulations used to evaluate the performance of octree discretization using the modified SBFEM. This section is divided into four subsections. First, an elastic beam is modelled, including shear and pure torsion forces on one end using four

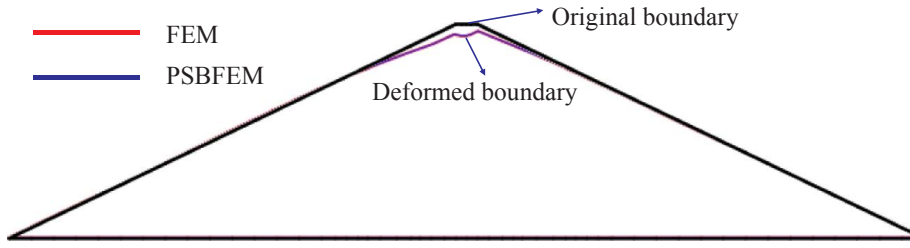


Fig. 24. The total deformation of the maximum cross-section after the earthquake ground motion ($10 \times$ magnification).

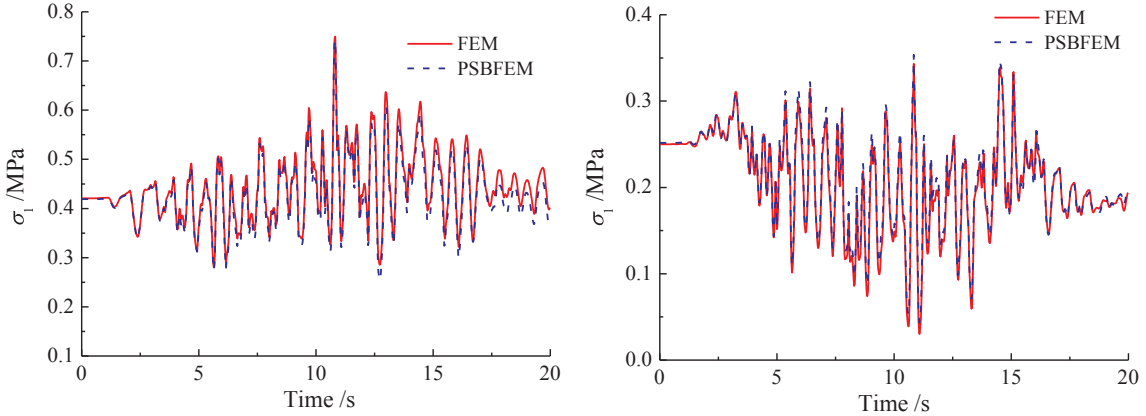


Fig. 25. Principal stress time-histories of Element B during the earthquake ground motion.

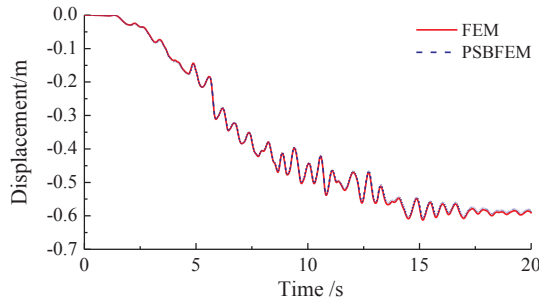


Fig. 26. Displacement time-histories of Point A during the earthquake ground motion in the y-direction.

levels of elements. Then, an elasto-plastic simulation is performed, and it is compared with the FEM to validate the proposed method. Finally, an engineering application using an automatic octree grid generator is presented.

6.1. Verification of the elastic beam

6.1.1. End-shear load

As a first step towards verifying the element behaviour, a cantilevered beam loaded in shear is studied to evaluate the performance of the NPSBFEM. The domain R for this problem is $(-0.5, 0.5) \times (-0.5, 0.5) \times (0, L)$, which is illustrated in Fig. 12. The load is a constant traction given by $S = [0, -F, 0]^T$ on the free end.

The displacement fields corresponding to these stresses up to the addition of a rigid body motion are provided in [42]. In this numerical study, the length of the beam was 5, the shear load was taken as $F = 0.1$, and the material was assumed to be homogeneous and isotropic with a Young's modulus $E = 500$ and Poisson's ratio $\nu = 0.3$.

The beam is fixed on the plane, where the coordinate z is zero. The bending loading condition due to an end-shear load was considered. An octree mesh was used. The following four levels of mesh refinement were considered: $N_x \times N_y \times N_z = 4 \times 4 \times 20$, $8 \times 8 \times 40$, $16 \times 16 \times 80$, and $32 \times 32 \times 160$. Clipped views of the four grid levels

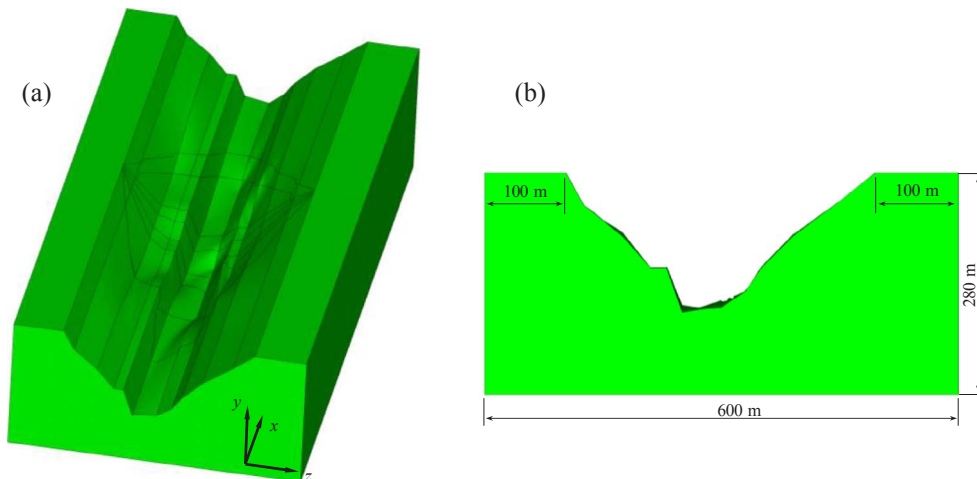


Fig. 27. Valley shape of the core wall dam: (a) three-dimensional view and (b) front view.

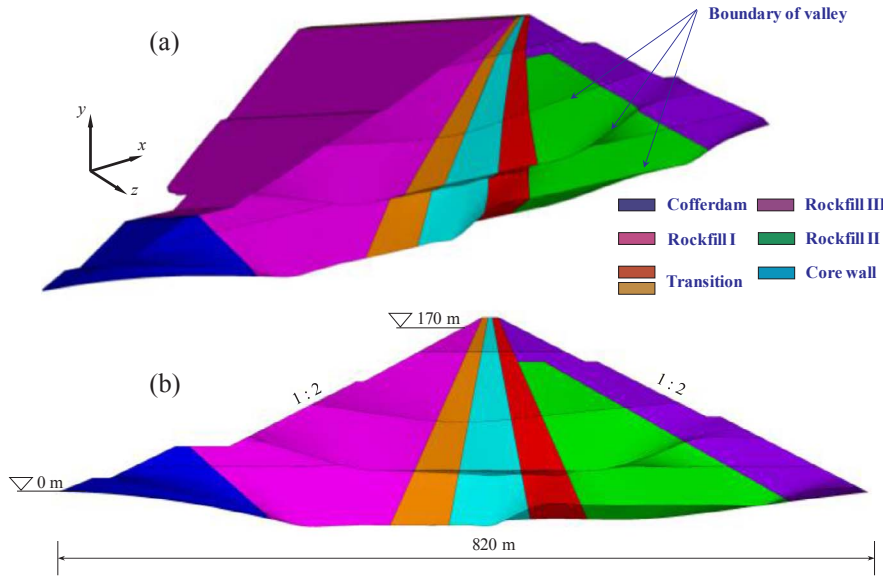


Fig. 28. Geometric dimensioning and material partitioning of the core wall dam: (a) three-dimensional view, (b) front view and (c) intersection lines of the material and valley.

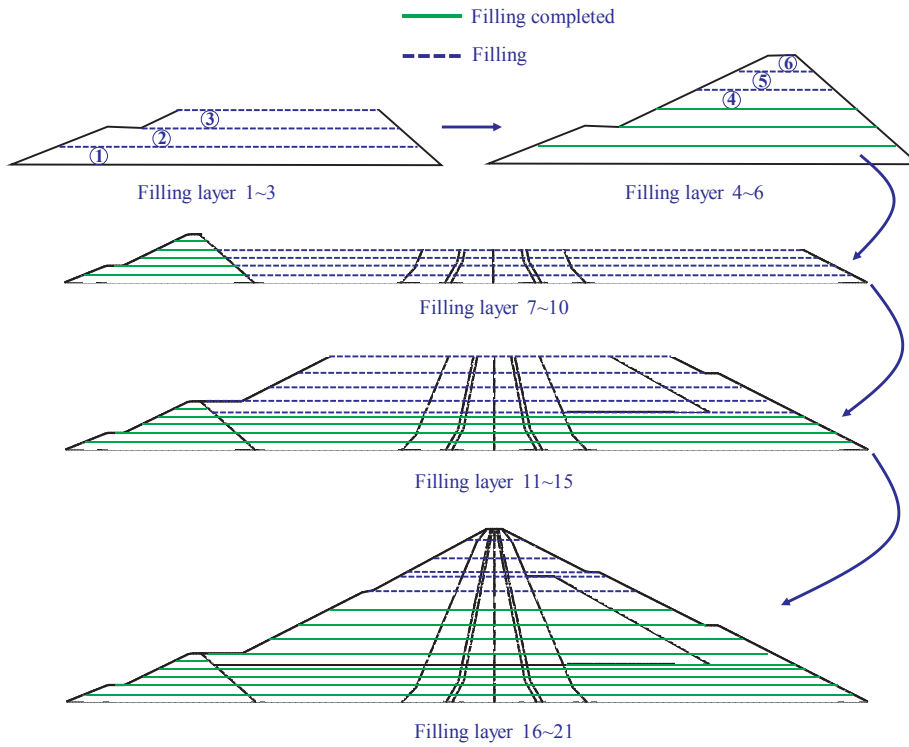


Fig. 29. Typical diagrammatic drawing of the layered construction.

are shown in Fig. 13. The numbers of elements and nodes are listed in Table 3.

Fig. 15 shows the von Mises stresses for the four levels of mesh refinement. The deformation pattern is consistent in the different meshes. The displacements are most similar to the theoretical asymptotic value with the finest mesh. The relative errors of the displacements are calculated from the maximum in the y direction using three integration schemes and are plotted in Fig. 14, where u is the calculated value, and u^* is the theoretical asymptotic value. The error decreased with an increasing number of elements. These results demonstrate that the proposed method is reasonable and valid.

6.1.2. Pure torsion

To investigate the applicability of the NPSBFEM in simulating

elastic torsion problems, numerical studies were conducted considering the deformation of the same beam in a torsion state. The analytical displacements for this problem up to rigid body motion are provided in [42].

The relative errors of the beam displacements in the y direction using the scheme presented above under the torsional load for different mesh levels are shown in Fig. 16.

Similarly, the von Mises stresses for the four mesh levels are shown in Fig. 17, where a uniform distribution can be observed in the different meshes. The results are more accurate when more grids are used. The result approaches the exact value with an increasing number of elements. The vulnerable region can easily be identified from the stress distribution, which can provide reasonable guidance for the structural design.

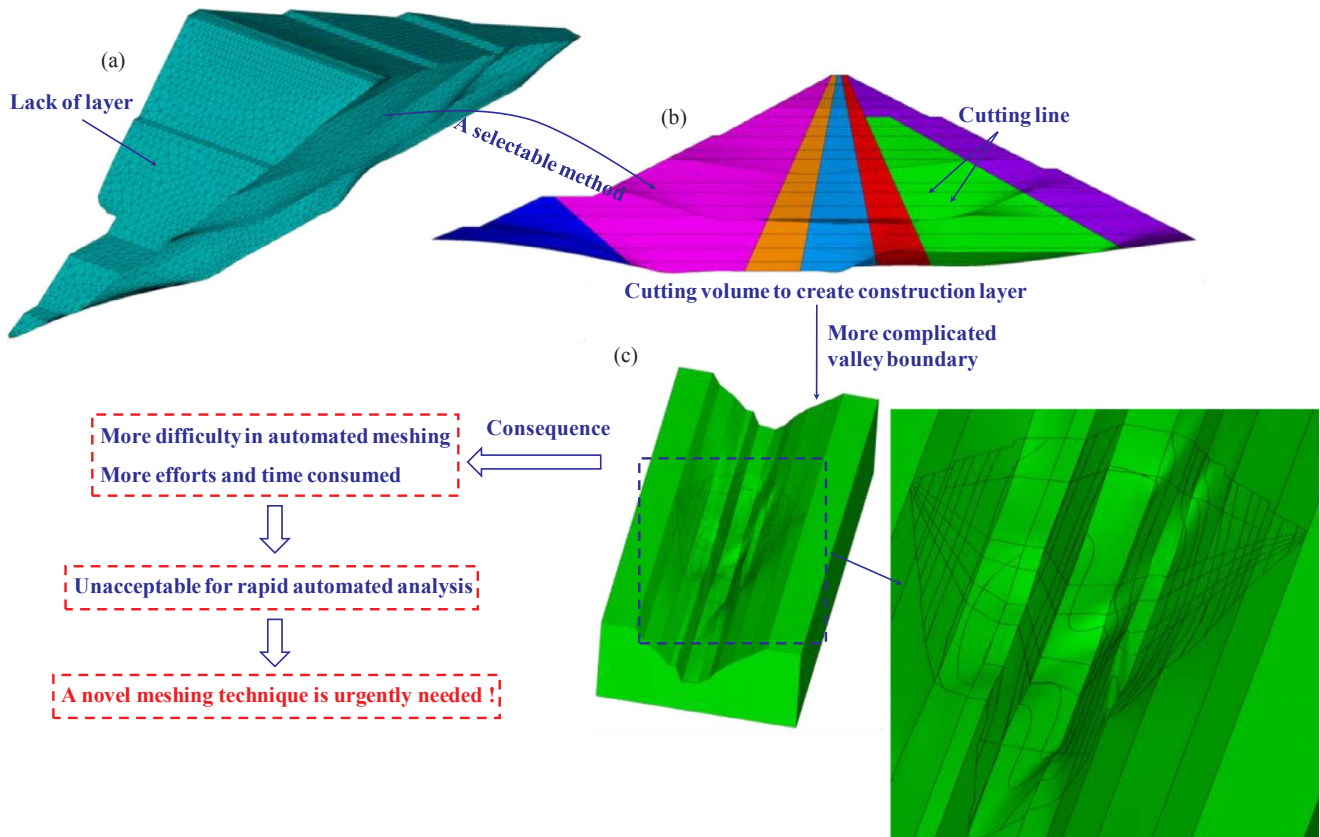


Fig. 30. Automatic mesh generation using tetrahedral elements: (a) tetrahedral grid, (b) front view of the cut volume and (c) valley intersection lines.

6.2. Verification of the elasto-plastic simulation

The modified SBFEM is now employed to investigate a nonlinear problem. To facilitate comparison, normal element types are selected, and the simulation is also modelled using the conventional FEM, which provides a reference solution. Furthermore, Scheme 3 is adopted when using the NPSBFEM in the following simulations.

6.2.1. Modelling

A typical symmetric 100 m core wall dam with upstream and downstream slopes of 1V:2H is studied in this research. The simple material distribution of the dam and the dam's dimensions are illustrated in Fig. 18, and the matched gridding is shown in Fig. 19. The construction process is simulated by controlling the birth and death of elements. The dam body is divided into 20 layers. The water level is then impounded to an elevation of 90 m in twenty steps.

6.2.2. Material parameter identification

A generalized plasticity model for the rockfill [43,44] is adopted, which was proposed in the literature [45,46]. The parameters are listed in Tables 4 and 5.

6.2.3. Input ground motions

An earthquake with maximum accelerations measured at the foundation gallery of 0.294 g, 0.196 g and 0.294 g in the x -, y - and z -directions, respectively, was considered. The acceleration records of the seismic wave are shown in Fig. 20; these records are used as the input motions with a time step of 0.02 s.

6.2.4. Results and discussion

(1) Static results

The displacements and stresses of the maximum cross-section after impoundment calculated using the two methods are illustrated in Figs. 21 and 22, respectively. The proposed method performs well; the results correspond well with those obtained from the FEM with only slight differences in some locations.

(2) Dynamic results

Next, the response of the core wall dam during the earthquake ground motion is discussed to validate the dynamic analysis. The final results on the maximum cross-section are displayed in Figs. 23 and 24, including the dynamic displacement and the total deformation after the earthquake ground motion. The results are consistent with each other, which implies that the modified method is appropriate for the seismic analysis of geotechnical engineering structures.

The time histories of Element **B** and Point **A** during the earthquake are shown in Figs. 25 and 26, respectively. Similarly, good consistency is revealed in these comparison diagrams. These comparisons with the FEM demonstrate that the modified PSBFEM is accurate.

6.3. Engineering application

The practical model of the core wall dam is more complex, and several important factors should be considered in the simulation, including the valley shape, material partitioning and effect of filling. Unfortunately, if these factors are considered simultaneously, it will be extremely difficult to rapidly generate a regular grid to be used in the conventional FEM; significant human efforts will be consumed in the pretreatments. Furthermore, the quality of the mesh cannot be guaranteed, and malformed elements typically emerge.

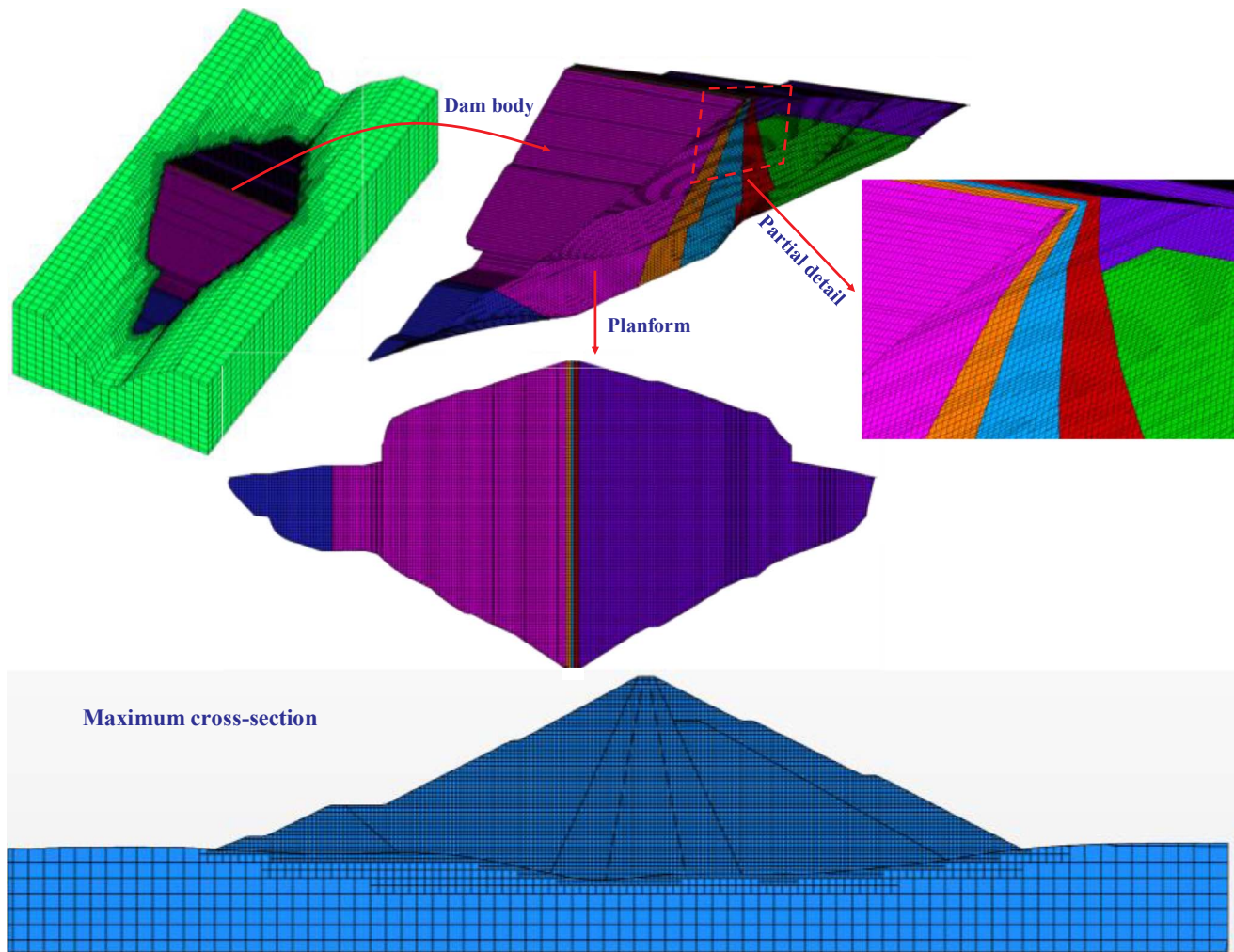


Fig. 31. Octree mesh of the core wall dam with materials marked: (a) the entire model and (b) the dam body.

Table 6
Statistics of the element types in the core wall model with an octree mesh.

Element types	Faces in one element	Number	Percentage (%)	Sum
Conventional element	4	1765	0.52	94.52
	5	30,386	8.93	
	6	289,515	85.07	
Polyhedron	> 6	18,667	5.48	5.48

6.3.1. Modelling

(1) Valley shape

The valley shape used in this simulation is shown in Fig. 27. As an introductory engineering application, an irregular valley is studied in this paper.

(2) Material partitioning

A typical dam consists of many materials. A representative partitioning is shown in Fig. 28, including the cofferdam, rockfill, transition, and core wall. The interfaces are critical to determining the regions of different materials, which lead to many boundary surfaces in the model. The model becomes more complex when the boundary surfaces intersect the valley, which is marked with yellow dashed lines. Similarly, the valley will become more complex with the intersection lines from the material, as shown in Fig. 28(c).

(3) Layered construction

Layered construction represents the construction sequence of the structure, and the effects of stratified construction (e.g., the height of each layer is the same), which is typically used in simulations, is adopted in this paper. A simple representative decomposition diagram is shown in Fig. 29.

It is extremely difficult to discretize this model using hexahedrons when the layered conditions are considered, and fully automatic generation is nearly impossible with this approach. Tetrahedrons can automatically accomplish the mesh generation, although the elements are not laminar. One method to resolve this problem is to create each layer beforehand by cutting the dam body. A representative diagram is shown in Fig. 30. Additional effort and time will be required, which in turn results in more elements and less automation. This is unacceptable for rapid automated analysis.

A rapid, efficient and fully automatic mesh generation technique and matching element type are imperative to address this problem.

(4) Rapid modelling

This paper introduces a rapid and efficient octree generator to address the difficulties presented above. The discretization has three primary features:

- ① The discretization is fast, and the process is automatic. Only

Spatial distribution of two element types

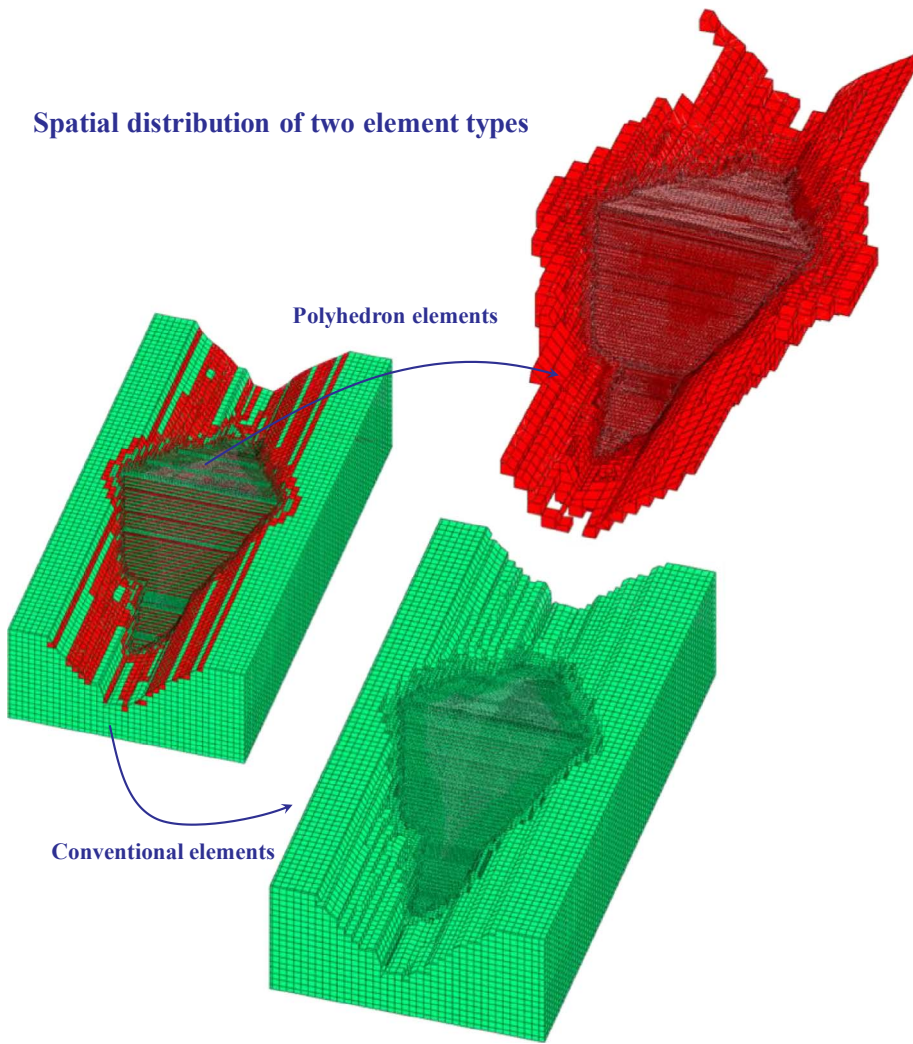


Fig. 32. Distribution of conventional elements and polyhedral elements.

Table 7
Transition material parameters in the modified generalized plasticity model.

G_0	K_0	M_g	M_f	α_f	α_g	H_0	H_{U0}	m_s
1200	1400	1.77	0.99	0.45	0.5	900	3000	0.5
m_v	m_l	m_u	r_d	γ_{DM}	γ_u	β_0	β_1	
0.5	0.4	0.5	50	50	4	24	0.045	

information about the volume, maximum element size and minimum element size is needed. Taking the dam analysed previously as an example, an octree grid with the material marked is illustrated in Fig. 31. The minimum and maximum sizes are 3.937 m and 15.748 m, respectively, which lead to 340,333 elements and 387,453 nodes, respectively. More importantly, the entire dissociation takes only 69.19 s, which dramatically accelerates the pre-treatment process compared with the current discretization method. ② In addition, the grid can be reconstructed rapidly, and the density can be determined in different regions if necessary. The number of computations can be decreased considerably. In addition, the process takes only a few minutes instead of the several days or weeks consumed by each new model using the conventional approach. ③ The third attractive characteristic is that most of the elements are conventional, which provides an excellent opportunity for coupled calculations. Simple statistics are listed in Table 6, which shows that the aforementioned core wall dam contains 321,669 traditional

elements, which represent 94.52% of the elements in the model (see Fig. 32).

Similar to the second example, the effect of the construction process is approximated by controlling the birth and death of elements. The dam body is divided into 54 layers. The water level is subsequently impounded to an elevation of 170 m in 34 steps.

6.3.2. Parameters

The generalized plasticity model is used to conduct static and dynamic analyses of the core wall dam. One of the advantages is that the parameters are identical throughout the entire simulation. To simplify the expression, the parameters for the core wall and rockfill are uniform and are given in Tables 4 and 5, respectively. The remaining materials are given in Table 7.

The seismic waves in three directions for the dynamic analysis are illustrated in Fig. 20. A detailed explanation is provided in Section 6.2.3; thus, this topic is not discussed further here.

6.3.3. Results

The final results are plotted in Figs. 33–37, including the distributions of the displacement and normal stress, the displacement and stress time histories and the total deformation after the earthquake. In summary, the overall distributions are reasonable, which implies that the proposed method is reliable in managing a complex engineering application.

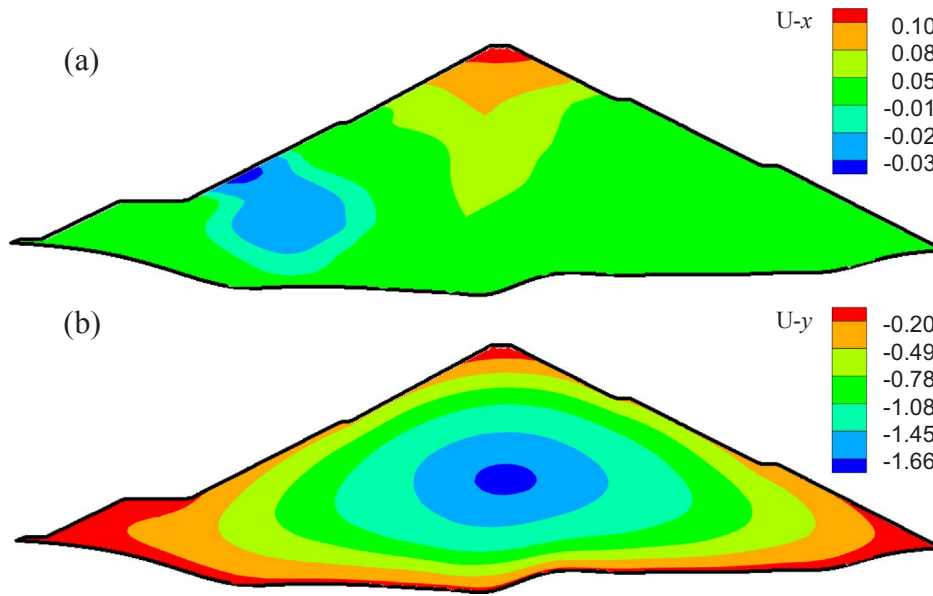


Fig. 33. Displacements of the maximum cross-section after impoundment (units: m): (a) x-direction and (b) y-direction.

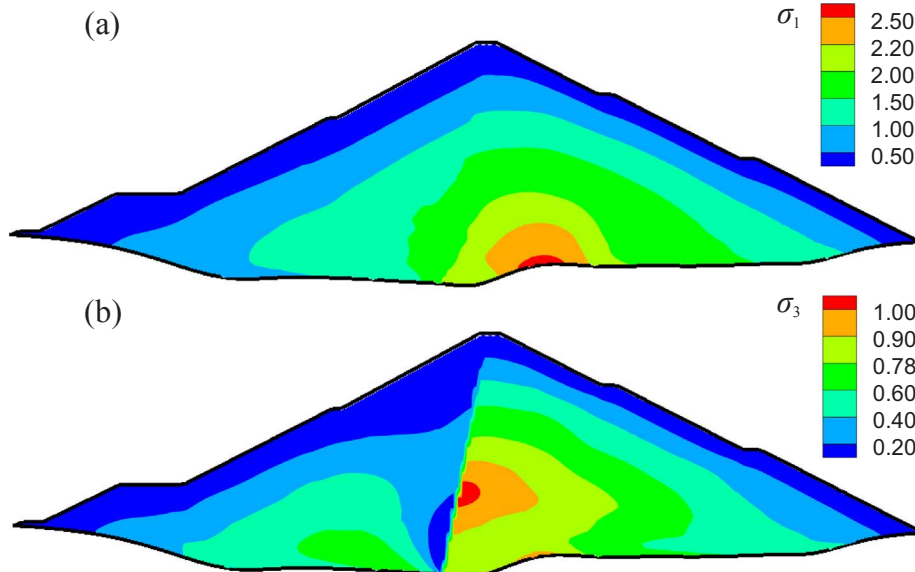


Fig. 34. Principal stresses of the maximum cross-section after impoundment (units: MPa): (a) maximum principal stress and (b) minimum principal stress.

7. Conclusions

This paper proposed a highly general nonlinear octree SBFEM for the rapid design and analysis of complex engineering structures. The shape functions and derivatives of the polygonal boundary elements are pre-calculated using mean-value interpolation. Subsequently, the polyhedral derivation is conducted as in the original SBFEM, whereas an internal integral strategy is adopted instead of an initial boundary integration scheme. Under these conditions, the advantages of the SBFEM and flexible polyhedrons are exploited, and the elasto-plastic analysis is performed.

Several numerical examples were presented to validate the accuracy and reliability of the method by comparing the results with the exact solutions for an elastic beam under a shear load and pure torsion. A simulation of a typical core wall dam was conducted, and the results were compared with those obtained from the FEM. The comparison demonstrates the good correspondence between the proposed method and the FEM. Finally, a more complex model was used to verify the feasibility and convenience of the proposed method. Three main conclusions can be drawn as follows:

1. The modelling pretreatment of complex geotechnical engineering structures is highly burdensome because it must consider many factors simultaneously. The problem can be greatly simplified using the octree discretization program presented in this paper. The efforts consumed in the pre-processing can be decreased dramatically because a high-quality grid can be created within a few minutes. Further engineering applications and rapid elaborate analyses for complex structures will be performed, and interesting phenomena could be revealed using the powerful technique.
2. Combined with a fully automatic octree generator, the polygonal boundary surfaces can be solved directly without secondary treatment. The method has more potential and is convenient and flexible for rapid adaptive design and analysis as well as cross-scale and multi-scale simulations based on the octree mesh.
3. The SBFEM has been extended to more fields with a more general library of element shapes. Elasto-plastic analyses can be performed as conveniently as with the FEM. The modified SBFEM will henceforth be free from nonlinear restrictions.

Further extensions will be developed in the future. The combination

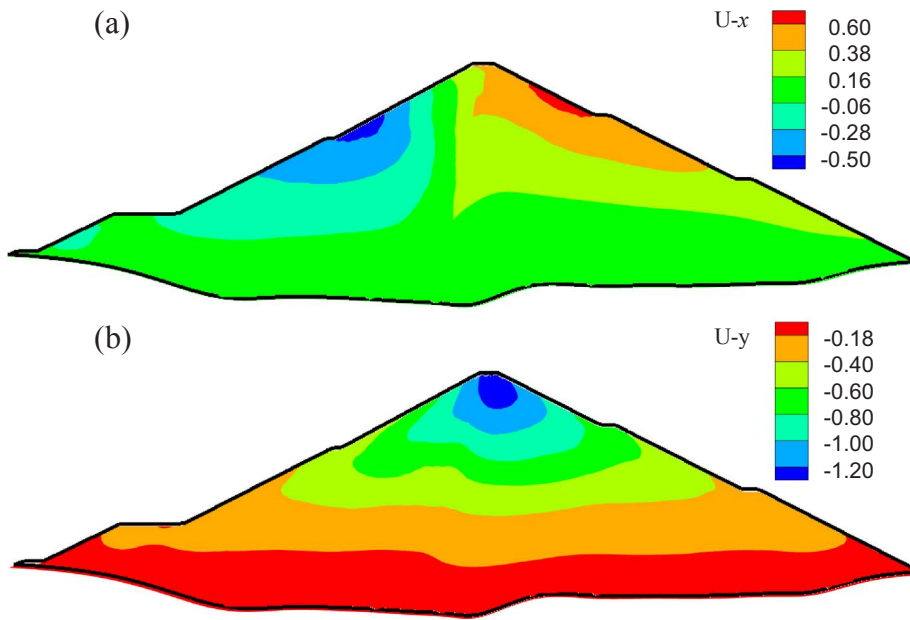


Fig. 35. Displacements of the maximum cross-section after the earthquake ground motion (units: m): (a) x-direction and (b) y-direction.

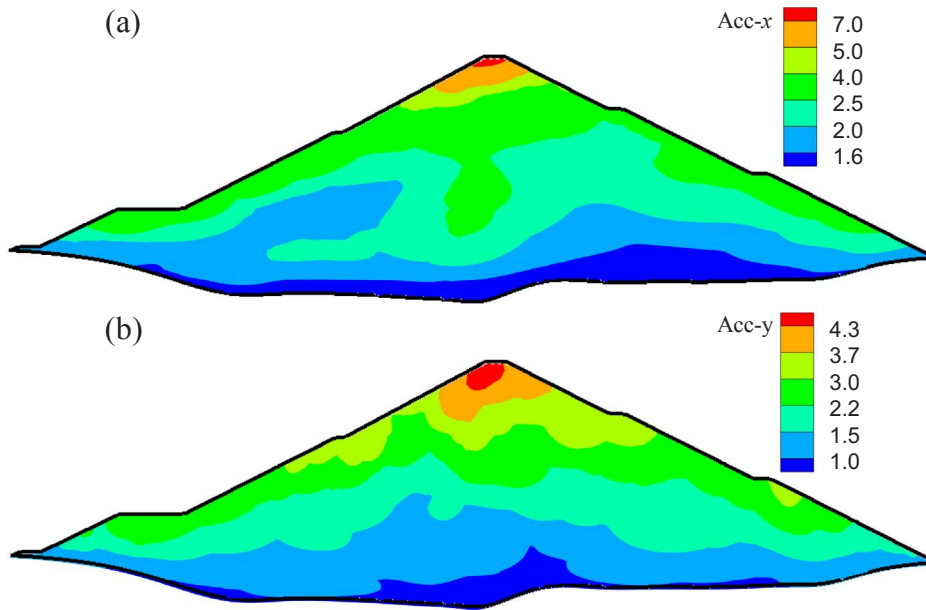


Fig. 36. Distribution of accelerations of the maximum cross-section after the earthquake ground motion (units: m/s²): (a) x-direction and (b) y-direction.

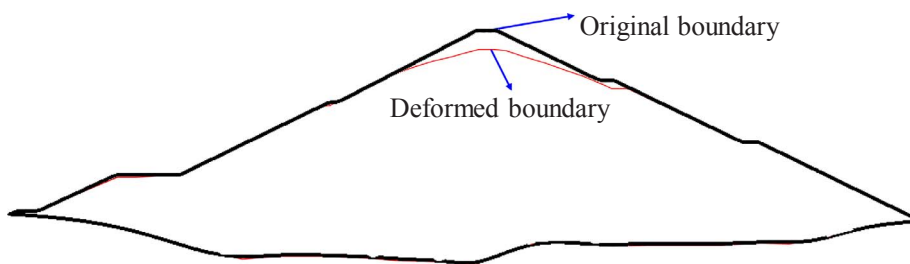


Fig. 37. Total deformation of the maximum cross-section after the earthquake ground motion (20× magnification).

of this technique with the FEM may improve the efficiency of the proposed method.

Acknowledgements

This work was supported by National Key R&D Program of China (2017YFC0404900) and the National Natural Science Foundation of

China (Grant Nos. 51421064, 51779034). The work is also supported by the Fundamental Research Funds for the Central Universities DUT17LK56. This financial support is gratefully acknowledged.

References

- [1] Frey PJ, George PL. Mesh generation. London, UK: ISTE; 2008.

- [2] Canann SA, Saigal S, Owen S J. Special edition on unstructured mesh generation. *Int J Num Meth Eng* 2000;1(49).
- [3] Field DA. The legacy of automatic mesh generation from solid modeling. *Comput Aided Geom Des* 1995;12(7):651–73.
- [4] Owen SJ. A survey of unstructured mesh generation technology. *IMR*; 1998. p. 239–67.
- [5] Shimada K. The 8th international meshing roundtable special issue: advances in mesh generation; 2001.
- [6] Viceconti M, Taddei F. Automatic generation of finite element meshes from computed tomography data. *Critical Reviews™ in Biomedical Engineering*; 2003; 31(1&2).
- [7] Liu Y, Saputra AA, Wang J, et al. Automatic polyhedral mesh generation and scaled boundary finite element analysis of STL models. *Comput Methods Appl Mech Eng* 2017;313:106–32.
- [8] Saputra A, Talebi H, Tran D, et al. Automatic image-based stress analysis by the scaled boundary finite element method. *Int J Numer Meth Eng* 2017;109(5):697–738.
- [9] Bishop JE. A displacement-based finite element formulation for general polyhedra using harmonic shape functions. *Int J Numer Meth Eng* 2014;97(1):1–31.
- [10] Natarajan S, Bordas S, Ooi ET. Virtual and smoothed finite elements: a connection and its application to polygonal/polyhedral finite element methods[J]. *Int J Numer Meth Eng* 2015;104(13):1173–99.
- [11] Gain AL, Talischi C, Paulino GH. On the virtual element method for three-dimensional linear elasticity problems on arbitrary polyhedral meshes. *Comput Methods Appl Mech Eng* 2014;282:132–60.
- [12] Manzini G, Russo A, Sukumar N. New perspectives on polygonal and polyhedral finite element methods. *Math Models Meth Appl Sci* 2014;24(08):1665–99.
- [13] Quey R, Dawson PR, Barbe F. Large-scale 3D random polycrystals for the finite element method: Generation, meshing and remeshing. *Comput Methods Appl Mech Eng* 2011;200(17):1729–45.
- [14] Wolf JP, Song CM. Finite-element modelling of unbounded media. Chichester: Wiley; 1996.
- [15] Wolf JP, Schanz M. The scaled boundary finite-element method. Chichester, U.K: Wiley; 2004.
- [16] Man H, Song C, Gao W, et al. A unified 3D-based technique for plate bending analysis using scaled boundary finite element method. *Int J Numer Meth Eng* 2012;91(5):491–515.
- [17] Lin Gao, Liu Jun, Li Jianbo, Hu Zhiqiang. A scaled boundary finite element approach for sloshing analysis of liquid storage tanks. *Eng Anal Boundary Elem* 2015;56:70–80.
- [18] Goswami S, Becker W. Computation of 3-D stress singularities for multiple cracks and crack intersections by the scaled boundary finite element method. *Int J Fract* 2012;175(1):13–25.
- [19] Hell S, Becker W. The scaled boundary finite element method for the analysis of 3D crack interaction. *J Comput Sci* 2015;9:76–81.
- [20] Saputra AA, Birk C, Song C. Computation of three-dimensional fracture parameters at interface cracks and notches by the scaled boundary finite element method. *Eng Fract Mech* 2015;148:213–42.
- [21] Birk C, Behnke R. A modified scaled boundary finite element method for three-dimensional dynamic soil-structure interaction in layered soil. *Int J Numer Meth Eng* 2012;89(3):371–402.
- [22] Liu Jun, Lin Gao. A scaled boundary finite element method applied to electrostatic problems. *Eng Anal Boundary Elem* 2012;36(12):1721–32.
- [23] Liu J, Zhang P, Lin G, et al. Solutions for the magneto-electro-elastic plate using the scaled boundary finite element method. *Eng Anal Boundary Elem* 2016;68:103–14.
- [24] Li Peng, Liu Jun, Lin Gao, et al. A NURBS-based scaled boundary finite element method for the analysis of heat conduction problems with heat fluxes and temperatures on side-faces. *Int J Heat Mass Transf* 2017;113:764–79.
- [25] Xu H, Zou D, Kong X, et al. Error study of Westergaard's approximation in seismic analysis of high concrete-faced rockfill dams based on SBFEM. *Soil Dynam Earthq Eng* 2017;94:88–91.
- [26] Chen K, Zou D, Kong X, et al. A novel nonlinear solution for the polygon scaled boundary finite element method and its application to geotechnical structures. *Comput Geotech* 2017;82:201–10.
- [27] Liu Jun, Lin Gao, Li Jianbo. Short-crested waves interaction with a concentric cylindrical structure with double-layered perforated walls. *Ocean Eng* 2012;40:76–90.
- [28] Lin, Zhi liang, Liao, et al. The scaled boundary FEM for nonlinear problems. *Commun Nonlinear Sci Numer Simul* 2011;16(1):63–75.
- [29] Bransch M, Lehmann L. A nonlinear HHT- α method with elastic-plastic soil-structure interaction in a coupled SBFEM/FEM approach. *Comput Geotech* 2011;38(1):80–7.
- [30] Chen K, Zou D, Kong X. A nonlinear approach for the three-dimensional polyhedron scaled boundary finite element method and its verification using Koyna gravity dam. *Soil Dynam Earthq Eng* 2017;96:1–12.
- [31] Wachspress EL. A rational finite element basis. New York: Academic Press; 1975.
- [32] Meyer M, Barr A, Lee H, et al. Generalized barycentric coordinates on irregular polygons. *J Graphics Tools* 2002;7(1):13–22.
- [33] Floater MS, Kós G, Reimers M. Mean value coordinates in 3D. *Comput Aided Geometric Des* 2005;22(7):623–31.
- [34] Hormann K, Floater MS. Mean value coordinates for arbitrary planar polygons. *ACM Trans Graphics (TOG)* 2006;25(4):1424–41.
- [35] Sukumar N, Tabarraei A. Conforming polygon finite elements. *Int J Numer Meth Eng* 2004;61:2045–66.
- [36] Ooi ET, Song C, Tin-Loi F. A scaled boundary polygon formulation for elasto-plastic analyses. *Comput Methods Appl Mech Eng* 2014;268:905–37.
- [37] Jackins C, Tanimoto S. Octrees and their use in the representation of three-dimensional objects. *Comp Graphics Image Process* 1980;14:249–70.
- [38] Yerry MA, Shephard MS. Automatic three-dimensional mesh generation by the modified-octree technique. *Int J Numer Meth Eng* 1984;20(11):1965–90.
- [39] Shephard MS, Georges MK. Automatic three-dimensional mesh generation by the finite octree technique. *Int J Numer Meth Eng* 1991;32(4):709–49.
- [40] Karman S, Betro V. Parallel hierarchical unstructured mesh generation with general cutting. In: 46th AIAA aerospace sciences meeting and exhibit; 2008. p. 918.
- [41] ITASCA Consulting Group Inc, KUBRIX Geo Version 15.0: advanced automatic and interactive grid generation for engineering software; 2016.
- [42] Barber JR. Elasticity. Springer, 3rd ed.; 2010.
- [43] Liu H, Zou D. Associated generalized plasticity framework for modeling gravelly soils considering particle breakage. *J Eng Mech* 2013;139:606–15.
- [44] Zou D, Xu B, Kong X, Liu H, Zhou Y. Numerical simulation of the seismic response of the Zipingpu concrete face rockfill dam during the Wenchuan earthquake based on a generalized plasticity model. *Comput Geotech* 2013;49:111–22.
- [45] Pastor M, Zienkiewicz OC, Chan AHC. Generalized plasticity and the modelling of soil behaviour. *Int J Numer Anal Meth Geomech* 1990;14:151–90.
- [46] Zienkiewicz OC, Chan AHC, Pastor M, Schrefler BA, Shiomi T. Computational geomechanics. Chichester: Wiley; 1999.